
Masters Theses

Student Theses and Dissertations

Spring 2008

Femtosecond laser micro-structuring of silicon wafer in water confinement

Songping Wu

Follow this and additional works at: https://scholarsmine.mst.edu/masters_theses



Part of the [Mechanical Engineering Commons](#)

Department:

Recommended Citation

Wu, Songping, "Femtosecond laser micro-structuring of silicon wafer in water confinement" (2008).
Masters Theses. 6853.

https://scholarsmine.mst.edu/masters_theses/6853

This thesis is brought to you by Scholars' Mine, a service of the Missouri S&T Library and Learning Resources. This work is protected by U. S. Copyright Law. Unauthorized use including reproduction for redistribution requires the permission of the copyright holder. For more information, please contact scholarsmine@mst.edu.

**FEMTOSECOND LASER
MICRO-STRUCTURING OF SILICON WAFER
IN WATER CONFINEMENT**

by

SONGPING WU

A THESIS

Presented to the Faculty of the Graduate School of the

MISSOURI UNIVERSITY OF SCIENCE AND TECHNOLOGY

In Partial Fulfillment of the Requirements for the Degree

MASTER OF SCIENCE IN MECHANICAL ENGINEERING

2008

Approved by

**Hai-Lung Tsai, Advisor
Hai Xiao
Darryl Alofs**

© 2008

Songping Wu

All Rights Reserved

ABSTRACT

This thesis investigates the use of femtosecond laser induced surface morphology on silicon wafer surface in water confinement. Unlike irradiation of silicon surfaces in the air, there are no laser induced periodic structures, but irregular roughness is formed when the silicon wafer is ablated under water. Interestingly, a particular parameter combination enables a smooth surface, which can improve the surface quality of micro-machining products.

This thesis first investigates the single ablation and multi-pulse ablation processes in order to study the effects of laser parameters on ablation morphology, as well as the basic physics and mechanism of the laser-material interaction process under water. Laser power, focal position, and laser pulse number are alternately varied to cause different levels of laser energy to be deposited onto the silicon surface. Interesting surface morphology phenomena, such as flower-like structures and co-central rings, are detected.

Next, femtosecond laser direct writing process in water confinement is investigated. By scanning the surface at different laser repetition rates and different laser powers, a good surface quality can be achieved at a certain threshold repetition rate combined with relatively low power levels. Post-processing, such as annealing and chemical etching, also alters the surface pattern, but not as pronouncedly as changing laser parameters.

The unique discovery of a smoothly processed silicon surface in water confinement under certain laser parameter combinations may help improve laser direct micro-machining surface quality in industrial applications.

ACKNOWLEDGMENTS

I would like to express my sincere gratitude to my advisor, Dr. Hai-Lung Tsai. His wide knowledge and his logical way of thinking have been of great value for me. His understanding, encouraging and personal guidance have provided a good basis for the present thesis.

I am deeply grateful to Dr. Hai Xiao. His detailed and constructive comments and his sparkling ideas in the experiments support me throughout this work. I also wish to express my warm and sincere thanks to Dr. Darryl Alofs for his guidance in fluid mechanics.

I warmly thank all the laser micro-machining lab group mates, Zhi Liang, Yukun Han, Rock Powell, Naveen and Bala, for their kind help on my experiments and thesis. I also wish to thank all the close friends in Rolla for giving me untiring help during my difficult moments. I am grateful to Summer and Birdie for polishing my thesis. I owe my sincere gratitude to my Christian Mom, Juanita. I owe my loving thanks to my beloved parents in China and my grandpa in heaven.

TABLE OF CONTENTS

	Page
ABSTRACT.....	iii
ACKNOWLEDGMENTS	iv
LIST OF ILLUSTRATIONS.....	vii
LIST OF TABLES.....	ix
SECTION	
1. INTRODUCTION	1
2. FEMTOSECOND-LASER INTERACTION WITH SILICON.....	3
2.1. FEMTOSECOND LASER ABLATION IN THE AIR	3
2.2. FEMTOSECOND LASER ABLATION IN WATER	6
2.3. EXPERIMENTAL SETUP.....	8
2.3.1. Laser System Setup.....	8
2.3.2. Beam Profile Test	10
2.3.3. Energy Power Output Test.....	11
3. FEMTOSECOND LASER ABLATION IN WATER	13
3.1. EFFECT OF LASER POWER	13
3.1.1. Test of Ablation Threshold	14
3.1.2. Laser Ablation with Different Laser Powers.	15
3.1.3. Calculation of Single Pulse Ablation Threshold and Laser Radius Focus	22
3.2. EFFECT OF FOCAL POSITION.....	24
3.3. EFFECT OF LASER PULSE NUMBER	32
3.3.1. Ablation SEM Result Analysis.....	33
3.3.2. Incubation Effect.....	37
3.4. SUMMARY OF LASER ABLATION IN THE WATER	39
4. FEMTOSECOND LASER-INDUCED SURFACE MORPHOLOGY IN WATER	40
4.1. EFFECT OF REPETITION RATE	41
4.1.1. SEM Analysis and Mechanism Discussion.	42
4.1.2. AFM Analysis and Applicability.	49

4.2. EFFECT OF LASER POWER	51
4.3. EFFECT OF ANNEALING AND ETCHING	55
4.3.1. Annealing	56
4.3.2. Chemical Etching	58
4.4. SUMMARY OF SURFACE MORPHOLOGY INDUCED BY LASER DIRECT WRITING	60
5. CONCLUSION AND OUTLOOK.....	63
BIBLIOGRAPHY	66
VITA.....	75

LIST OF ILLUSTRATIONS

Figure	Page
2.1. Schematic of the different morphological phenomena after irradiation on the silicon surface with linearly polarized femtosecond laser pulses of 100 fs duration.....	5
2.2. Schematic of the laser-induced plasma in the confined region by characterizations of the shock wave in the target.....	8
2.3. A schematic of femtosecond laser setup for micro-structuring.....	9
2.4. Specimen setup in water confinement.....	10
2.5. Beam profile of femtosecond laser.....	11
3.1. SEM images of femtosecond laser-induced Si surface morphology irradiated in deionized water.....	15
3.2. SEM images of femtosecond laser-induced Si surface morphology irradiated in air.....	17
3.3. Schematic illustration of two regions of surface damage.....	20
3.4. Tilted view of surface morphology after single laser pulse ablation in the air at 0.6 mJ.....	21
3.5. Square diameters versus laser energy ratio for treatment of silicon in water.....	23
3.6. Schematic of focal position experiment setup.....	24
3.7. SEM images of surface morphologies after one laser pulse in water for the target position.....	25
3.8. SEM images of surface morphologies after one laser pulse in air for the target position.....	27
3.9. Shock wave propagation underneath the material surface.....	31
3.10. SEM images of ablation morphology at 0.042mJ/pulse in water.....	34
3.11. SEM images of ablation morphology at 0.042mJ/pulse in air.....	35
3.12. Graph of diameter squared as a function of log of the laser pulse number of 1, 5, 10, 50, 100, 250, 500, 1000 respectively both in the water and the air.....	38
4.1. Femtosecond laser surface scanning tracks.....	41
4.2. SEM images of femtosecond laser-induced surface morphology in water.....	43
4.3. SEM images of femtosecond laser-induced surface morphology in the air.....	45
4.4. EDS analysis of silicon surface processed in the air	46
4.5. EDS analysis of silicon surface processed in the water	47

4.6. Absorption coefficient of water versus wavelength.....	48
4.7. AFM picture of the surface irradiated by 0.14mJ/pulse femtosecond laser at 100Hz in water confinement	50
4.8. V-shape grooves fabricated by fs laser direct writing.....	50
4.9. SEM images surface pattern formed in water by laser energy	52
4.10. SEM images surface pattern formed in air by laser energy	54
4.11. SEM images of microstructures on silicon surface in the air.....	56
4.12. SEM images of microstructures on silicon surface in the water.....	57
4.13. EDS analysis of the processed surface after annealing	58
4.14. SEM images of microstructures on silicon surface in the air	59
4.15. SEM images of microstructures on silicon surface in the water	60
4.16. EDS analysis of the processed surface after etching.....	60

LIST OF TABLES

Table	Page
2.1. Power output check result.....	12
3.1. Working parameters for laser power experiment in water.....	14
3.2. Working parameters for focal position experiment in water.....	25
3.3. Working parameters for laser pulse number experiment in water.....	32
4.1. Working parameter list for laser repetition experiment in water.....	42
4.2. Working parameter list for laser power experiment in water.....	51

1. INTRODUCTION

It is well-known that the femtosecond pulses have two major advantages to micromachining over other longer pulse lasers in micro-machining: (i) the reduction of the pulse energy, which is necessary to induce ablation for fixed laser wavelength and focusing conditions and (ii) a significant reduction or complete removal of the heat-affected zone (HAZ) and, as a consequence, the improvement of the contour sharpness for the laser-processed structures [Besner et al., 2005]. Femtosecond lasers already possess a great range of applications, including optical-electronics, Micro-Electro-Mechanical Systems (MEMS) fabrication and biomedical application, with some of the richest being in materials science.

Second only to oxygen in earthly abundance, silicon is the most common semiconductor used in microelectronics and photonics and is produced in higher volume for lower cost than any other semiconductor. Its readily grown oxide rendered silicon the best choice for the semiconductor device industry. Its interactions with femtosecond laser in various kinds of environments have been widely studied [Carey, 2004].

This dissertation focuses on femtosecond laser processing of silicon in water confinement, a novel processing method used in the area of micro-machining. Water plays a role in self-cleaning and self-focusing. It largely influences the effect of laser absorption, which leads to distinguishable surface morphologies on silicon wafer as compared to the morphologies obtained in the air.

This thesis is organized as follows. Section 2 briefly reviews femtosecond laser micro-structuring. It also provides schematics of the experimental setup, especially the

femtosecond laser system setup. Moreover, experiments procedures are introduced in this chapter.

Section 3 examines the effect of experimental parameters on surface morphology after ablation in water. Femtosecond laser energy, focus position, and number of pulses have great impacts on the structure morphology formed on a silicon wafer. Possible mechanisms of femtosecond laser ablation in water confinement have been discussed in this chapter.

Section 4 examines the surface pattern on the silicon wafer after scanning by femtosecond laser pulse trains in water confinement. The effect of experimental parameters on the surface pattern has been examined via various material surface analysis methods, such as Scanning Electronic Microscope (SEM), Energy Dispersive Spectroscopy (EDS), and Atomic Force Microscope (AFM).

Section 5 summarizes the work included in this dissertation and comments on areas of future research. Research conclusions indicate that femtosecond laser micro-structuring in water confinement has innumerable great potential future applications.

2. FEMTOSECOND-LASER INTERACTION WITH SILICON

As lasers became capable of generating shorter and shorter pulses, it was necessary to improve the understanding of laser-material interactions. In comparison to continuous wave lasers, ultra-short pulsed lasers achieve much higher intensities. Their interactions with matter have distinct differences. The unique interaction of femtosecond lasers pulses with materials has given birth to extensive and productive research areas over the past couple of decades [Cerami et al., 2007].

2.1. FEMTOSECOND LASER ABLATION IN THE AIR

Femtosecond laser-induced surface morphology depends largely on the parameters involved in laser ablation, including the number of incident laser pulses, laser fluence, wavelength, pulse duration, and the ambient gas [Tull et al., 2006].

According to the report by Tull et al., the formation of the morphology on the Si surface irradiated by laser fluence above the ablation threshold can be separated into two parts, an early stage (1-10 pulses) and a late stage (>10 pulses). The first pulse causes small defects that are randomly distributed. After the second pulse, a distinct ripple pattern appears. During late-stage formation, from pulse 10 to several hundred pulses, conical microstructures with caps at their tips were created. Similar results were shown in the laser ablation of TiN on silicon (Bonse et al., 1999), and the height of the spikes was observed to grow with an increasing number of laser pulses, while the period remained the same. When irradiated by a large number of pulses (60,000) with a laser fluence much lower than the ablation threshold, sub-wavelength ripples were detected on

crystalline Si surface. With an even larger accumulation of pulses (120,000), typical wavelength-scale ripples were produced [Costache et al., 2004].

Laser fluence is another critical factor that affects the surface morphology. Reportedly, at lower fluence near the ablation threshold, sub-wavelength structures could be generated in SiC and Si and classical ripples occurred with the fluence above the threshold [Kautek et al., 2005]. With laser fluences higher than the ablation threshold, spike structures were detected on Si surfaces irradiated by 500 laser pulses in SF₆ atmosphere, and spike separation increased sharply with increasing laser fluence. Below the ablation threshold, no spikes were observed; the surface only showed ripples of sub-micro periodicity. Below the melting threshold, the surface always remained intact [Her et al., 2000, Bonse et al., 2002]. When the laser pulse energy is increased to a certain threshold, a bump-like structure appeared on the gold surface. Then, starting from a higher threshold, the nano-jets are formed [Korte et al., 2003, Korte et al., 2004].

Basically, the laser energy parameters, i.e., the number of laser pulses and laser fluence, largely determine the pattern on the laser irradiated surface [Bonse et al., 2002]. Figure 2.1 shows the typical surface morphology under different laser fluence and pulse number combinations.

It has also been reported that the period of the surface pattern is proportional to the femtosecond laser wavelength [Yasumaru et al., 2005, Riedel et al., 2004, Her et al., 2006]. Moreover, laser polarization orientation affects the shape and the direction of the surface pattern [Yasumaru et al., 2003, Yasumaru et al., 2005].

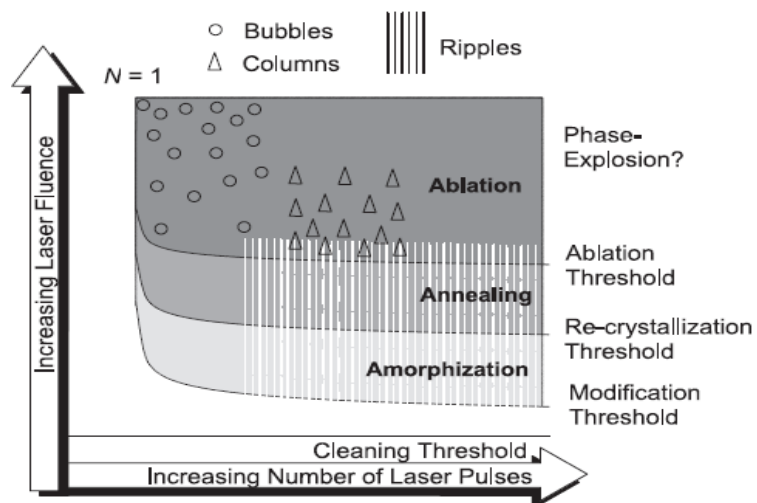


Figure 2.1. Schematic of the different morphological phenomena after irradiation on the silicon surface with linearly polarized femtosecond laser pulses of 100 fs duration

Researchers usually attribute wavelength-scale ripples to the mechanism of interference and subsequent local field enhancement [Guosheng et al., 1982, Jost et al., 1986]. However, this explanation has been ruled out by recent research. A self-organization theory that the spontaneous structure formation is caused by the strong temperature gradients combined with the strong electric field of the pulses has been put forth [Seifert et al., 2005]. A re-deposited mechanism explains the formation of spikes and the spherical shape of the caps suggests that they are due to the re-solidification of the liquid-silicon drop before the liquid can wet the sharp spike [Tull et al., 2006]. The chemical reaction is regarded as essential to shaping sharp or blunt spikes [Her et al., 1998]. Capillary waves and laser-induced etching are proposed to explain the spike formation in water [Shen et al., 2004]. The formation of sub-wavelength ripple structures is attributed to the out-of-phase superposition of electromagnetic fielded from the laser

pulses [Ozkan et al., 1999]. It is also explained by thermal oxidation of surface: the formation of dioxide changes the mechanical and optical properties of the irradiated area [Bonse et al., 2000]. Some researchers regard ripple formation as a non-thermal transition process and argue that the incubation effect plays an important role in sub-wavelength ripple formation process [Miyazaki et al., 2005]. Laser induced surface melting and re-solidification processes leads to nanojet structures [Korte et al., 2004]. However, no reassuring explanations can confirm the mechanism.

2.2. FEMTOSECOND LASER ABLATION IN WATER

Material laser processing in water has been preferred to the common dry treatment for specific technological applications for years. Quite recently, however, the idea of femtosecond laser micromachining under water has been developed. Eric Mazur et al. once irradiated a silicon surface that was submerged in water with 400 nm, 100 fs laser pulses focused by a 0.25 m focal-length lens and travelling through 10 mm of water before striking the surface at normal incidence. Sub-micrometer silicon spikes that are less than a micrometer tall and about 200 nm wide were fabricated, which were much smaller than the ones obtained in air [Shen et al., 2004]. Other researchers found that the ablation depths are lower and modification thresholds are higher than in the dry experiment. Ripple structures formed at the edges of the modified area showed a spacing of 100 nm for water, but 700nm for air experiments [Daminelli et al., 2004]. Later research showed that the ablation threshold and crater characteristics were similar for both water and air at low laser fluences, suggesting an identical radiation-related mechanism of material removal [Besner et al., 2005]. For laser ablation application, micrometer-sized bumps of several microns were formed on a glass surface using a

focused 800 nm, 150 fs repetition rate femtosecond laser processing in water [Hayasaki et al., 2007]. It has also been reported that channels with diameters in the order of tens of microns, high aspect ratios, and good wall-surface quality were machined in the presence of water [Hwang et al., 2004].

In most cases, water convection and bubble motion contributed to the removal of debris, leading to cleaner and more precise laser machining. The high heat capacity of water provides a better heat sink, thereby effectively cooling heat sensitive substrates and the ejected material [Daminelli et al., 2004].

Some researchers tried to explain the fundamental physical aspects of the underwater ablation process. According to Fabbro et al.'s studies, the laser-induced plasma induced a shock wave in the plasma plume due to the confinement of liquid. The laser-induced plasma expanded at a supersonic speed to create a shock wave in water. It absorbed the later part of the laser pulse and received a continual supply of the vaporizing species from the solid target. The shock wave induced extra pressure in the laser-induced plasma. This pressure increase is called the plasma-induced pressure. Then, the plasma-induced pressure caused an additional temperature increase of the laser-induced plasma. Thus, the shock wave pushed the laser-induced plasma into a thermodynamic state of the higher temperature, higher pressure, and higher density in comparison to the initially generated plasma by creating the additional pressure and temperature increases in the laser-induced plasma [Yang et al., 2007]. Figure 2.2 shows the schematic of the laser-induced plasma in water and the shock wave in the specimen.

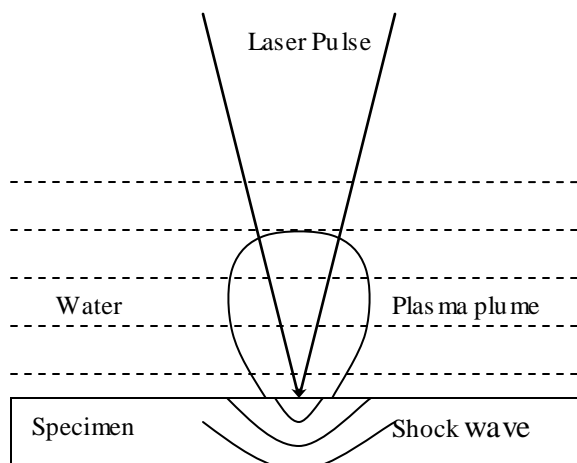


Figure 2.2. Schematic of the laser-induced plasma in the confined region by characterizations of the shock wave in the target

2.3. EXPERIMENTAL SETUP

The specifics of the experiments are described in details in each individual chapter. All of the experiments are conducted on silicon (110) wafers. A brief summary of the experimental system setup follows.

2.3.1. Laser System Setup. The laser used in our experiments is a regeneratively amplified, femtosecond Ti:sapphire system with a central wavelength of 800nm. The laser pulse width is 120 fs and the raw beam diameter is 6mm. The average laser power output is 1W. Amplified femtosecond laser pulses passed through a 300nm – 3000nm frequency conversion, a half wave plate, a polarizer and a series of ND filters, then is focused by an objective lens (NA 0.3-0.9) with a focal size of about 1 μ m in diameter on the sample surface. The sample is loaded onto a five-axis stage. Also, a coaxial CCD camera is set up from the top view of the sample surface in order to aid focusing and manufacturing process monitoring. A schematic of the system is shown in Figure 2.3.

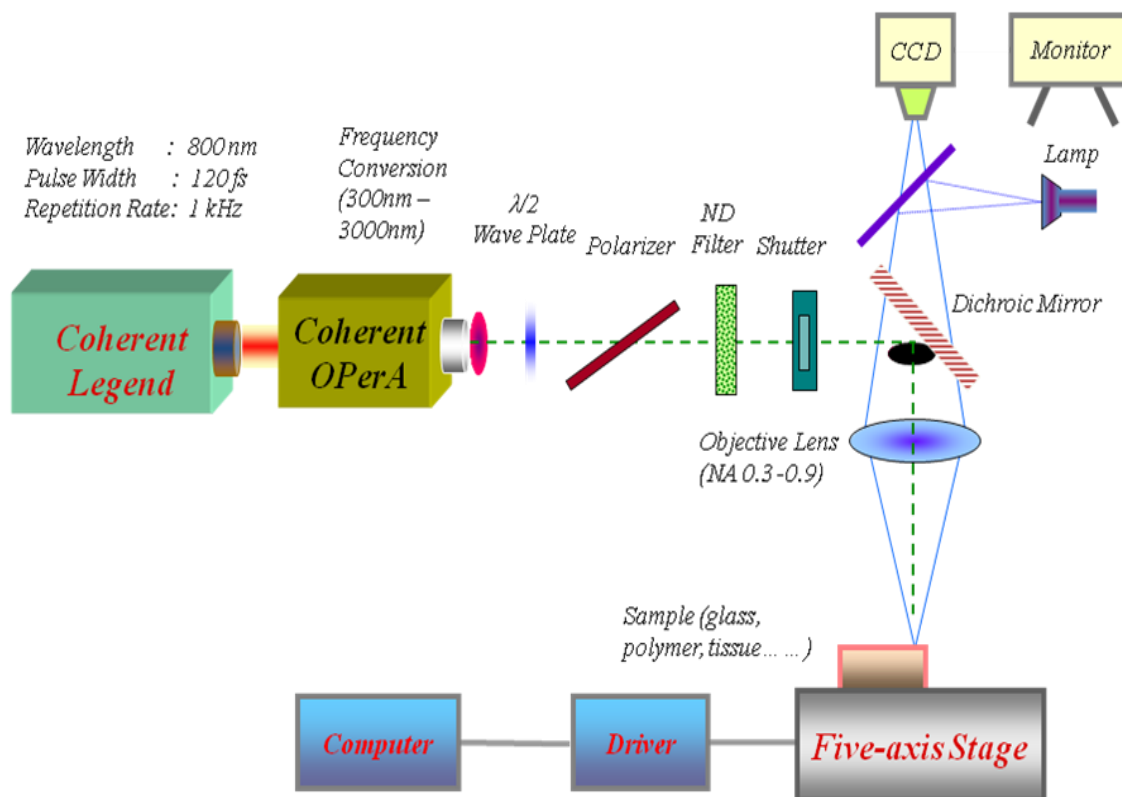


Figure 2.3. A schematic of femtosecond laser setup for micro-structuring

Figure 2.4. illustrates how femtosecond machining in liquid confinement was carried out and how the specimen was set up in liquid. As shown, an empty liquid container is pre-loaded to the stage. The specimen was fixed to the bottom of the container so as to make it stable relative to the stage. Then, de-ionized water was added to the container to cover the surface of the specimen. Concerning the optical lengths of the objective lens, the depth of water should be less than 3mm. The focus on the specimen surface and was regard as the focus of femtosecond laser pulses. Although the wavelengths of the guide light and laser were different to some extent, the thickness of the water was too thin to consider this difference.

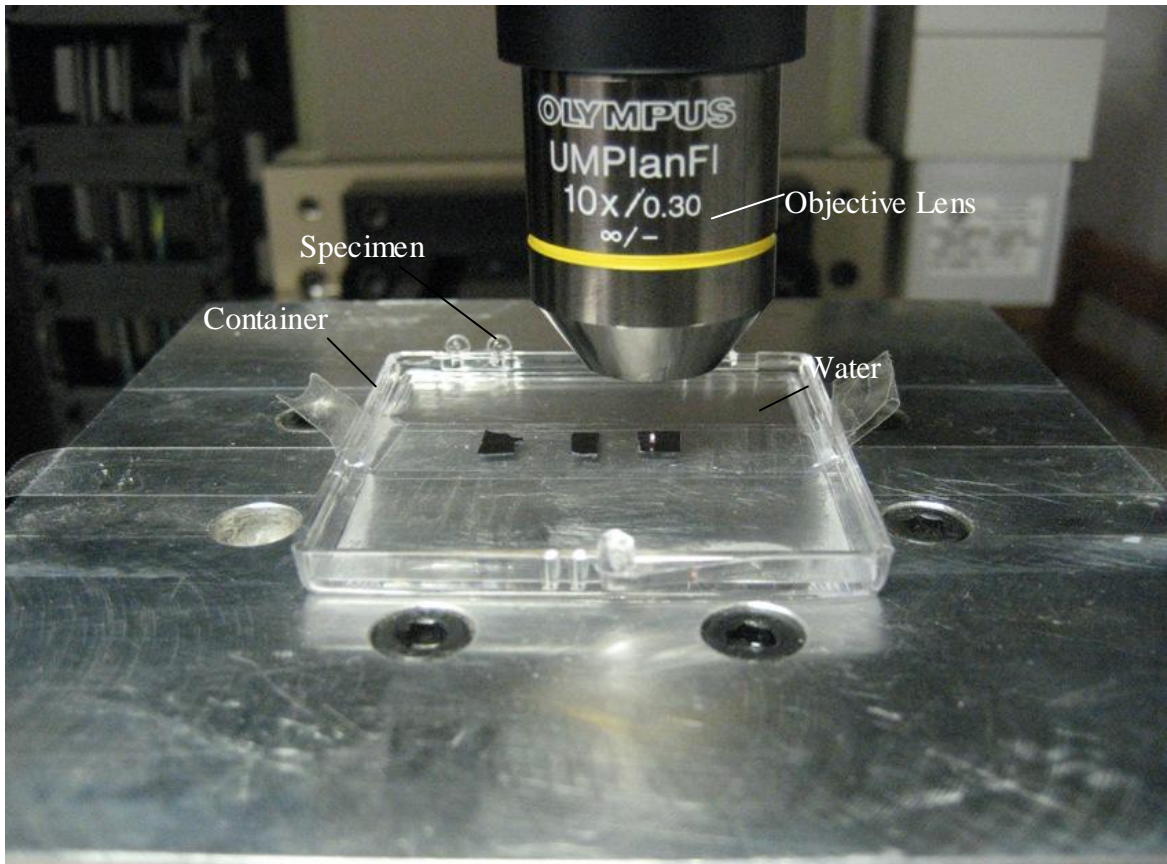


Figure 2.4. Specimen setup in water confinement

2.3.2. Beam Profile Test. A typical beam profile before objective lens focus was measured with a laser beam profiler (SPIRICON LBA-PC Series), as shown in Figure 2.5. The energy distribution does not appear as theoretical Gaussian distribution lines. It may be caused by many effects such as non uniform heating, laser medium and optics turbulence in the index matching fluid, etc. However, considering the requirement of laser micro-machining experiments in this thesis, the beam profile was acceptable for application.

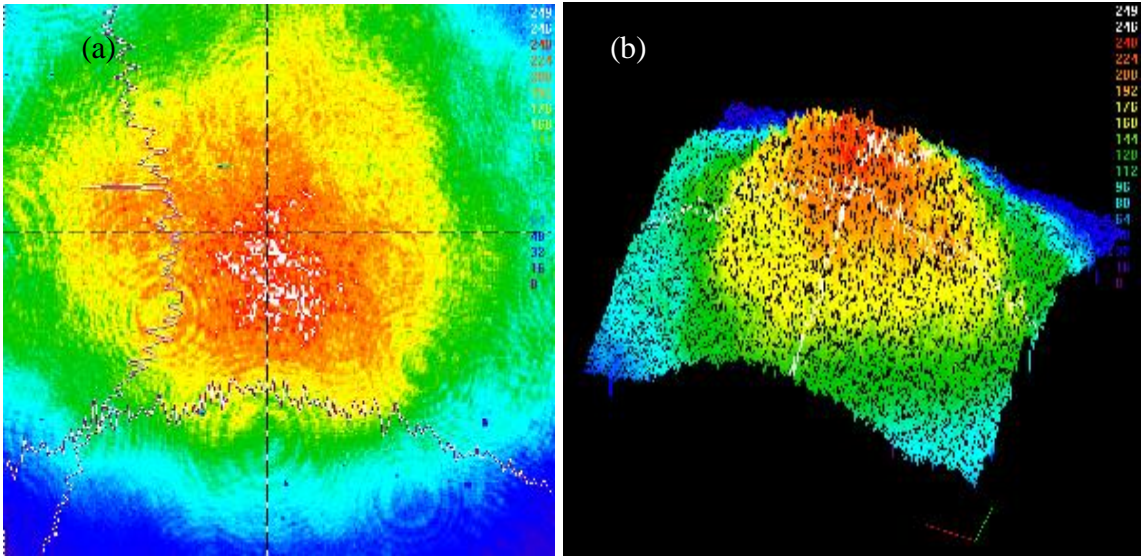


Figure 2.5. Beam profile of femtosecond laser (a)2D, (b)3D

2.3.3. Energy Power Output Test. A laser power/energy analyzer was used to check the output laser power before and after laser machining experiments. Table 2.1 lists the test results. The theoretical laser power of the raw beam should be 1W. Values of 0.97W and 0.96W were obtained before and after experimenting. Although energy loss was inevitable, the more important power intensity utilized in the experiments, was the beam after going through half wave plate. Since the raw beam energy was too high to be an appropriate source for micro-machining, the half wave plate was applied to lower the power to a usable scale. For our material, 0.02W is a preferable value for manufacturing. Paid attention to the stability of the laser power after the half wave plate, before and after experimenting, the power value after the half wave plate is identical according to our test results.

Table 2.1. Power output check result

Before Experiment		After Experiment	
Raw Beam	Beam after Half wave plate	Raw Beam	Beam after Half wave plate
0.97 W	0.02 W	0.96W	0.02W

3. FEMTOSECOND LASER ABLATION IN WATER

The surface morphology depends strongly on the parameters involved in femtosecond laser irradiation, including the number of incident laser pulses, laser fluence, wavelength, pulse duration, and the ambient gas (or liquid) species and pressure [Tull et al., 2006]. In order to effectively control the morphology, it is essential to determine the correlation between laser parameters and surface pattern features.

The experimental procedure described in this chapter involves three major variable parameters: laser energy, focal position and number of laser pulses. The extent to which these parameters impact and the surface morphological features obtained from ablation under water was studied. The results have been compared with those that were acquired in the air environment. This analysis sheds light on the possible formation mechanism of surface micro/nano-scale structures.

3.1. EFFECT OF LASER POWER

This section examines how the femtosecond laser power influences surface features. Other parameters are kept constant, while only the laser power was varied so as to obtain comparable results. If the laser power is very low, the surface may remain intact. However, as it goes above a certain value, visible ablation phenomenon can be detected. This specific laser power is called as the ablation threshold. The ablation threshold was tested in water for silicon and ablation experiments were carried out by applying a series of laser powers from the ablation threshold to a relatively high power. Moreover, ablation

results in air and in water were explicitly compared. Table 3.1 lists all the parameters used for the laser power experiment in water confinement.

Table 3.1. Working parameters for laser power experiment in water

Laser power (mJ/pulse)	6, 4.8, 4.2, 3, 2, 1.0, 0.6, 0.3, 0.2, 0.1, 0.042, 0.03
Pulse Number	1
Water Layer Thickness (mm)	0.8
Focal Position (mm)	0 (right at the surface)
Objective Lens	20 X

3.1.1 Test of Ablation Threshold. The ablation threshold largely depends on the number of pulses. For a single pulse ablation, the ablation threshold for silicon (110) wafer in the water confinement was 0.03mJ. By way of contrast, one pulse femtosecond laser ablation experiment was also conducted in the air. In this case, the ablation threshold tested was 0.03mJ, which is identical to the outcome obtained in the water. There are three possible explanations for this phenomenon. First, although the light absorption coefficient in water is 0.03/cm, which is pretty much larger than that in air, the thickness of the water layer is only 800 μm . Therefore, the energy absorbed is actually not considerable. Second, the laser energy is very low because only one single pulse near the ablation threshold is used. Although water confinement affects the interference between the laser-material interaction processes, its effect is negligible compared to high power

ablation or multi-pulse ablation, in which cases the water layer largely impacts the interaction. Another reason is that the thickness of water layer is only 1 mm and the laser beam is intensively focused by the objective lens. Although water plays a role in beam self-focusing, it is not very obvious in this case. Therefore the ablation thresholds tested for both environments are quite close to each other. A previous study showed that ablation threshold in water and in air are not the same [Daminelli et al., 2004], but the focal length of its objective used was at least 60mm, while the focal length applied here was only 3.1 mm.

3.1.2. Laser Ablation with Different Laser Powers. Figure 3.1 (a)-(l) are SEM images of silicon wafer surface after single pulse ablation in the water by 12 different laser powers. Figure 3.2 (a)-(l) show the ablation results with the same laser parameters, but conducted in the air.

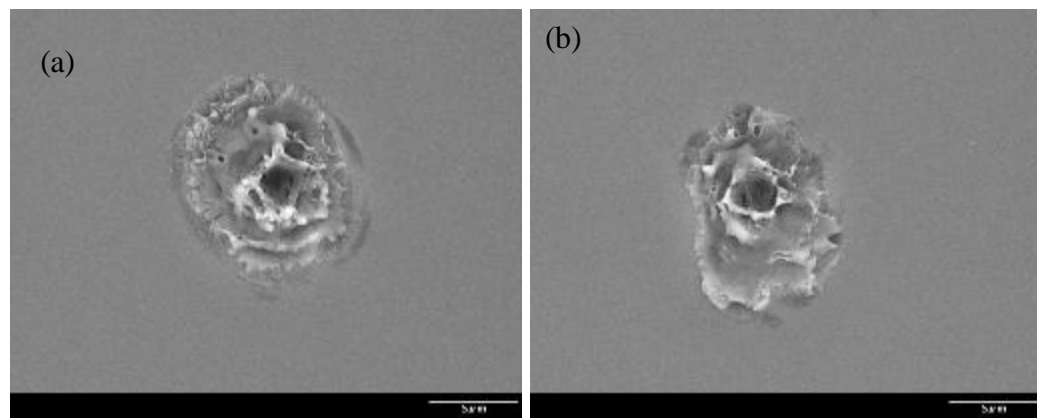


Figure 3.1. SEM images of femtosecond laser-induced Si surface morphology irradiated in deionized water (a) 6mJ, (b) 4.8 mJ, (c) 3 mJ, (d) 2 mJ, (e) 1.0 mJ, (f) 0.6 mJ, (g) 0.3 mJ, (h) 0.2 mJ, (i) 0.1 mJ, (j) 0.06mJ, (k) 0.042 mJ and (l) 0.03 mJ.

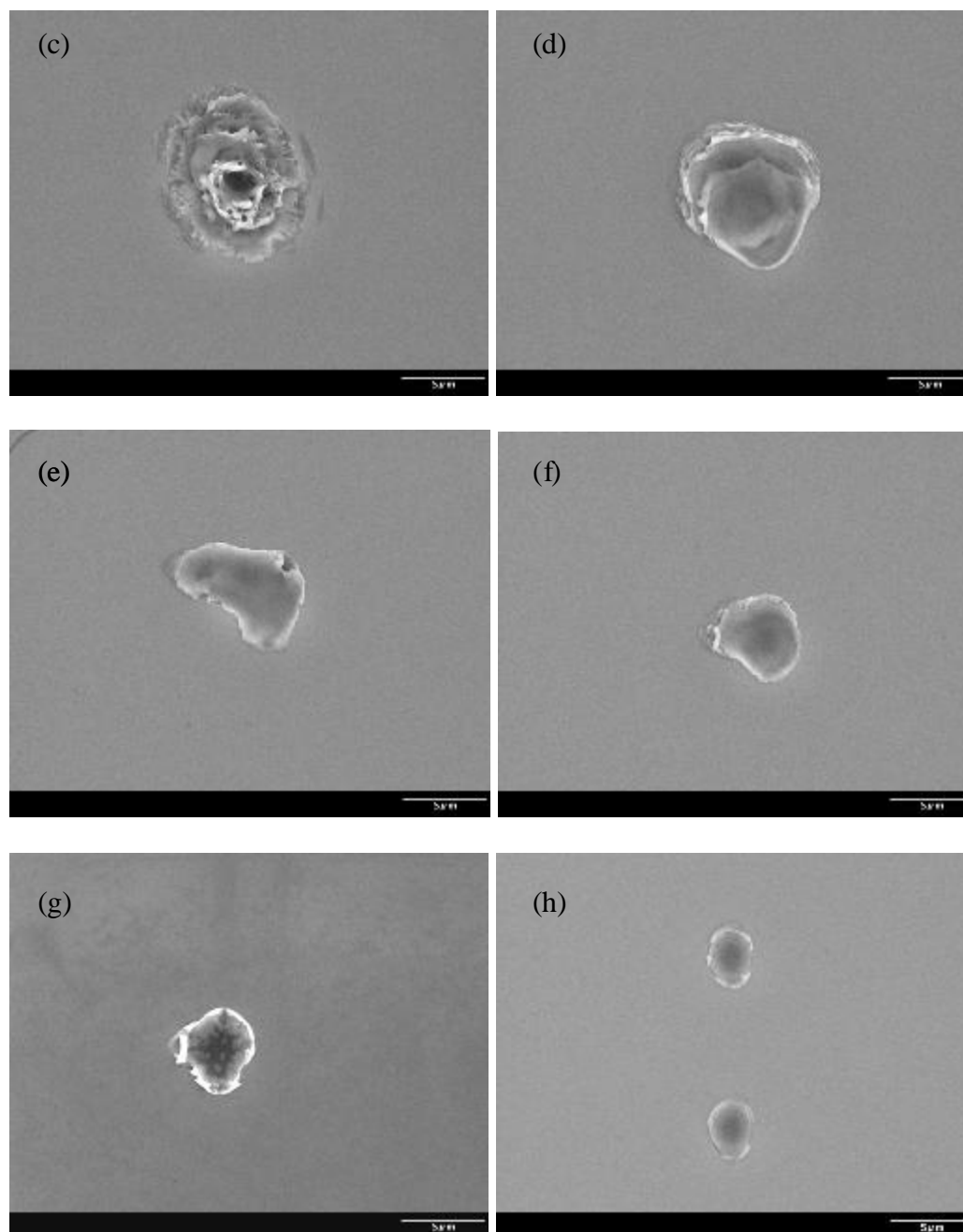


Figure 3.1. SEM images of femtosecond laser-induced Si surface morphology irradiated in deionized water (a) 6mJ, (b) 4.8 mJ, (c) 3 mJ, (d) 2 mJ, (e) 1.0 mJ, (f) 0.6 mJ, (g) 0.3 mJ, (h) 0.2 mJ, (i) 0.1 mJ, (j) 0.06mJ, (k) 0.042 mJ and (l) 0.03 mJ. (cont.)

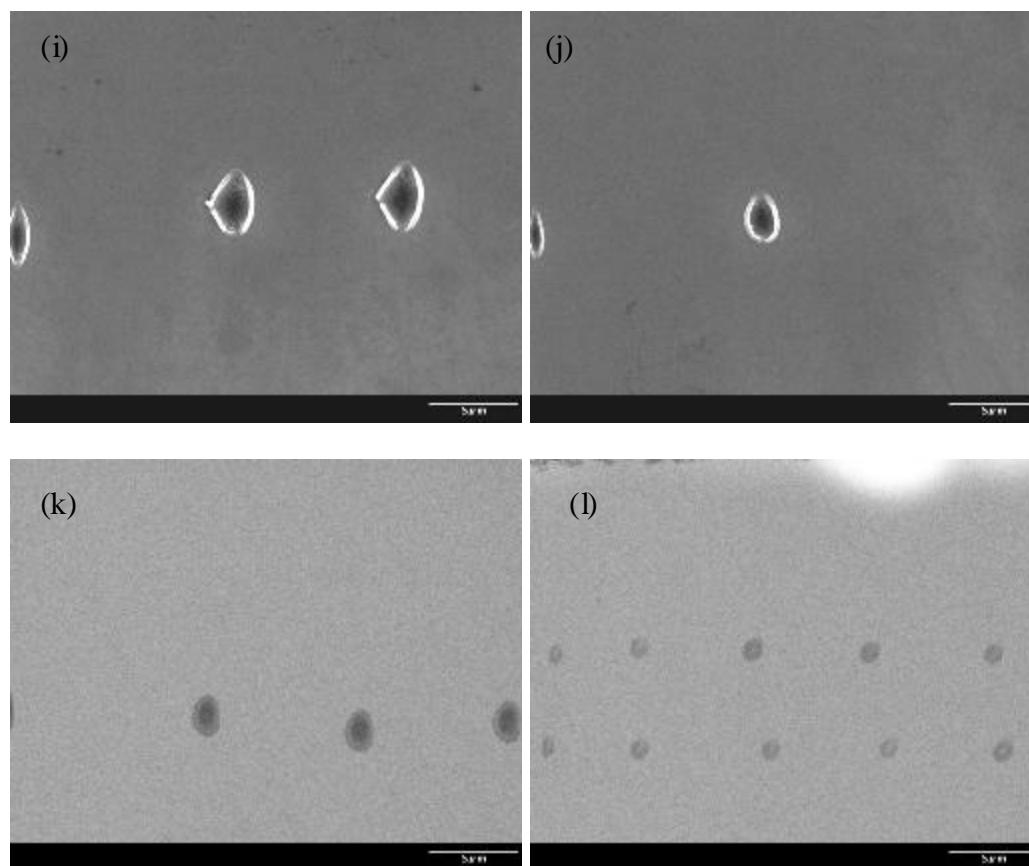


Figure 3.1. SEM images of femtosecond laser-induced Si surface morphology irradiated in deionized water (a) 6mJ, (b) 4.8 mJ, (c) 3 mJ, (d) 2 mJ, (e) 1.0 mJ, (f) 0.6 mJ, (g) 0.3 mJ, (h) 0.2 mJ, (i) 0.1 mJ, (j) 0.06mJ, (k) 0.042 mJ and (l) 0.03 mJ. (cont.)

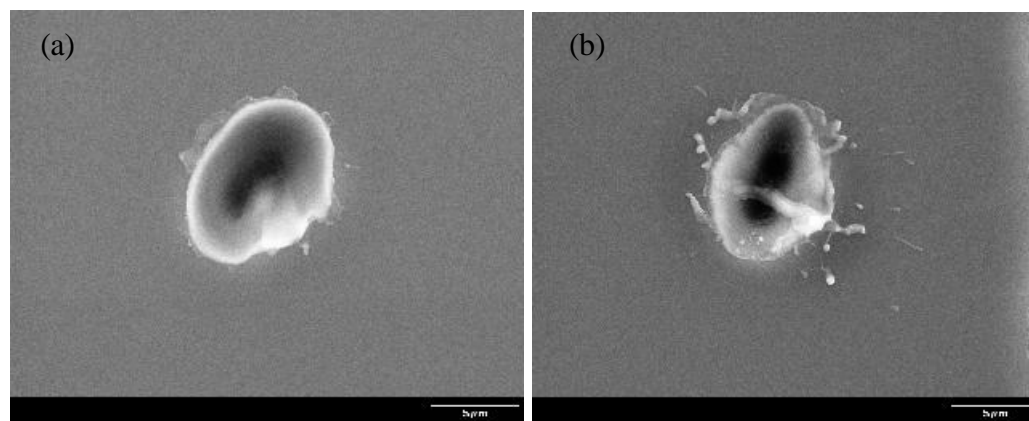


Figure 3.2. SEM images of femtosecond laser-induced Si surface morphology irradiated in air (a) 6mJ, (b) 4.8 mJ, (c) 3 mJ, (d) 2 mJ, (e) 1.0 mJ, (f) 0.6 mJ, (g) 0.3 mJ, (h) 0.2 mJ, (i) 0.1 mJ, (j) 0.06mJ, (k) 0.042 mJ and (l) 0.03 mJ.

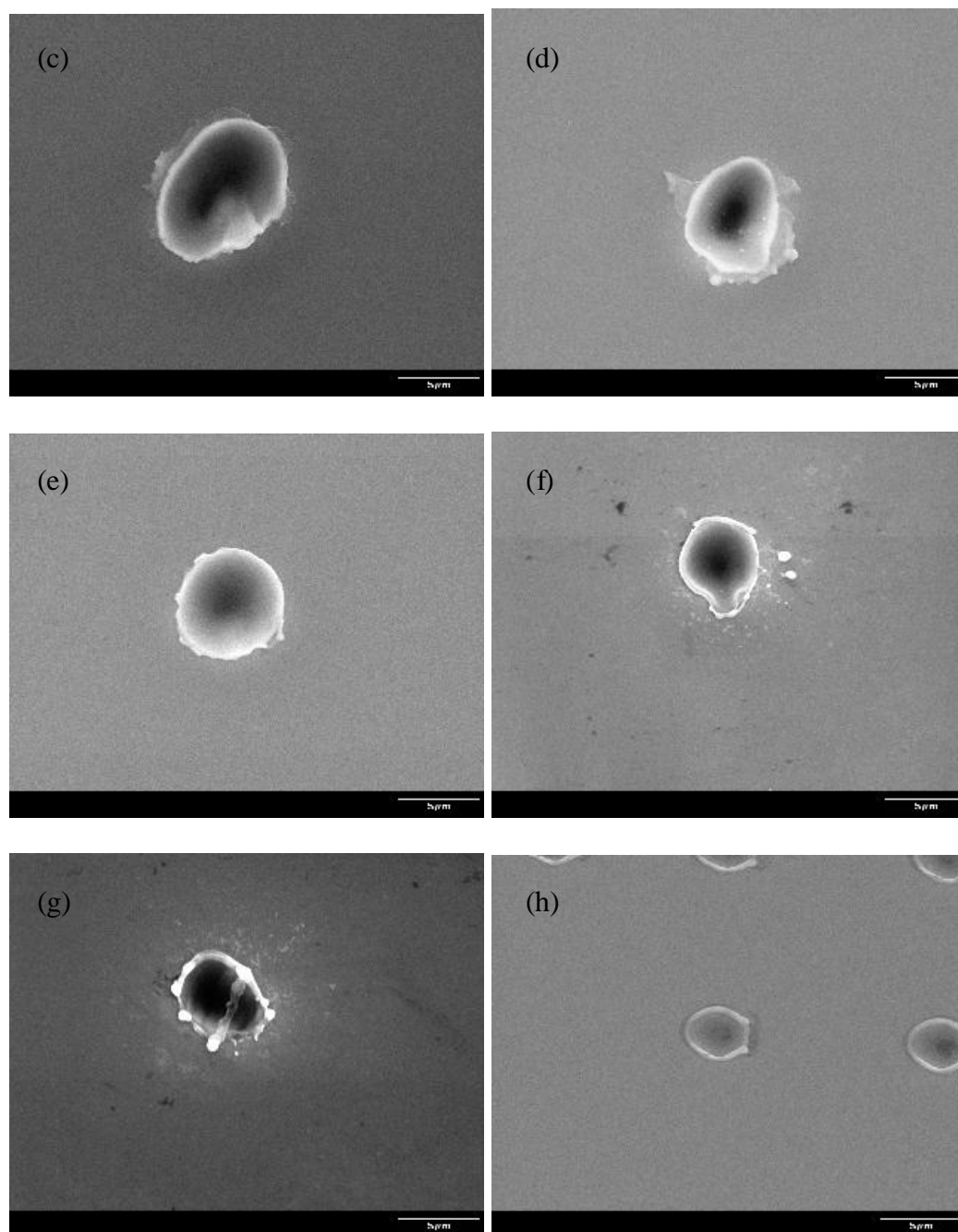


Figure 3.2. SEM images of femtosecond laser-induced Si surface morphology irradiated in air (a) 6mJ, (b) 4.8 mJ, (c) 3 mJ, (d) 2 mJ, (e) 1.0 mJ, (f) 0.6 mJ, (g) 0.3 mJ, (h) 0.2 mJ, (i) 0.1 mJ, (j) 0.06mJ, (k) 0.042 mJ and (l) 0.03 mJ. (cont.)

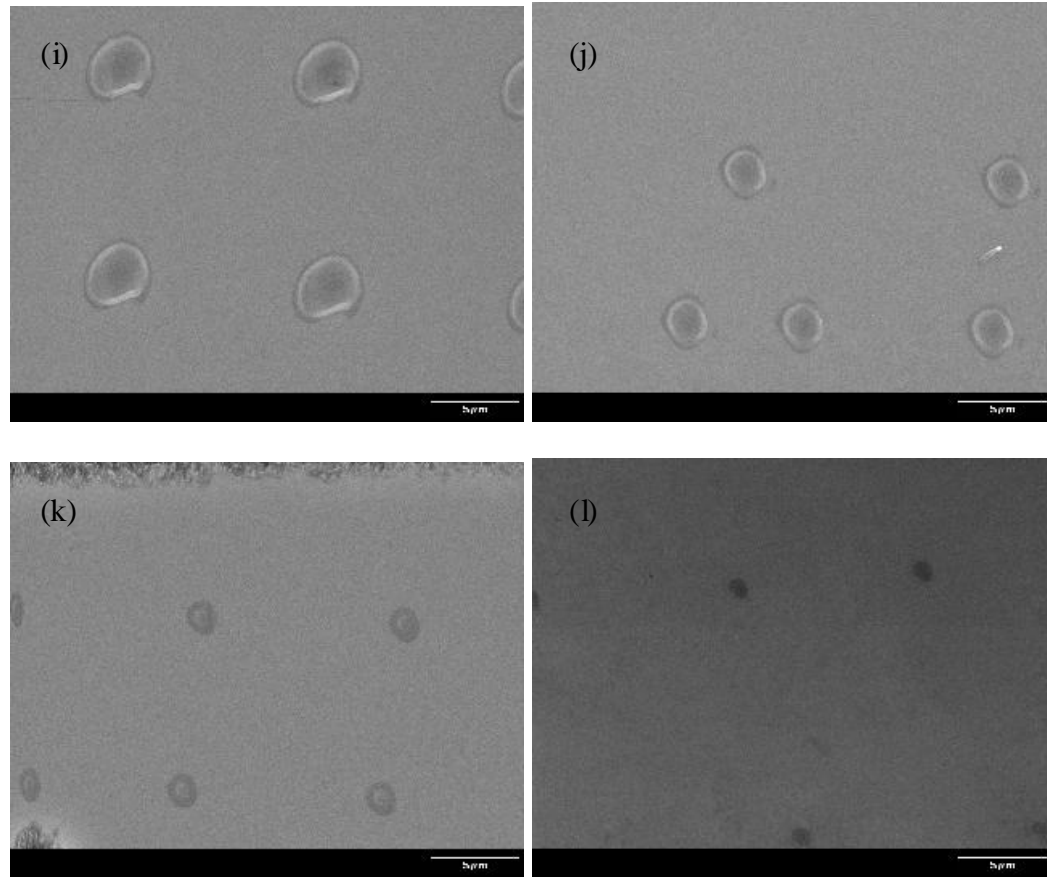


Figure 3.2. SEM images of femtosecond laser-induced Si surface morphology irradiated in air (a) 6mJ, (b) 4.8 mJ, (c) 3 mJ, (d) 2 mJ, (e) 1.0 mJ, (f) 0.6 mJ, (g) 0.3 mJ, (h) 0.2 mJ, (i) 0.1 mJ, (j) 0.06mJ, (k) 0.042 mJ and (l) 0.03 mJ. (cont.)

As the laser power changes from 0.03mJ to 2mJ (low power level) the surface damage morphologies featured two regions either in water or in air. Figure 3.3 is a schematic illustration of different regions of surface damage morphologies. The first zone is the center of the spot, which shows material removal as a result of the Gaussian beam's peak intensity. Ablation is caused by the transformation of a superheated layer into gas bubbles composed either of single atoms or of several molecular species. Consequently, a crater is formed on the surface [Dong et al., 2003]. The second zone is the border rim. This region is expected to be in the amorphous states or polycrystalline silicon since there

is a difference in the reflectivity shown in SEM images. The formation of amorphous or polycrystalline silicon is a kinetic process of material re-solidification. Since the cooling rate is fast during the solidification process (10^{14} °C/s), the melted material has no time to return to a crystalline state [Tran et al., 2005].

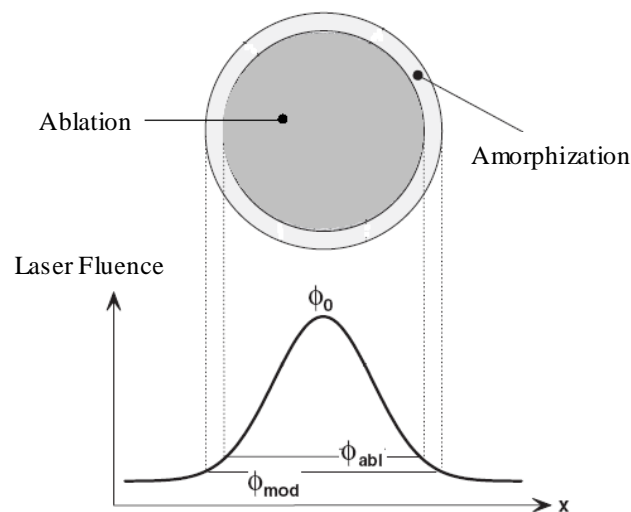


Figure 3.3. Schematic illustration of two regions of surface damage

Some researchers regard the outside rim region as outer modification and consider the phase change to occur because the energy fluence reaches the modification threshold due to the diffraction of laser beam [Tran et al., 2005]. This explanation is proved wrong according to the experiment results shown in Figure 3.4. It is easy to see that the outer rim protrudes out of the surface like a crater edge. If the outer rim is caused by laser-induced breakdown, it should appear as a round pit but not a protruding crater edge.

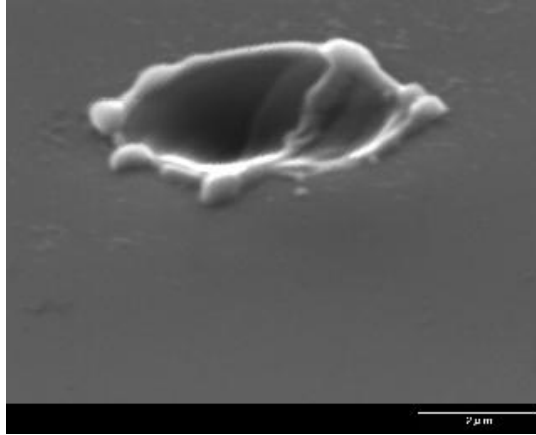


Figure 3.4. Tilted view of surface morphology after single laser pulse ablation in the air at 0.6 mJ

As compared to the low power level, when the laser power varied from 3 mJ to 6 mJ, surface damage morphologies for ablation in the air appeared to be distinctively different from ablation in water, as shown in images Figure 3.1 (a)-(d) and Figure 3.2 (a)-(d). In air, the surface morphology appeared as a two-region crater-like shape, as at the lower power. However, the diameter of the outer rim obviously expanded as the power increased.

Although the material removal in the central region was prominent, rough corrugations appeared around the central crater when the laser power reached 3 mJ. Plenty of rough corrugations become accumulated in the shape of a flower when the laser power was raised to the level of 4.2 mJ to 6 mJ. This special type of amorphous phase may be caused by the particular properties of laser ablation in liquids. The laser-material interaction in water is known to be accompanied by an energy transfer from plasma to the nearby water layer, causing vaporization of water and formation of bubbles. These bubbles then quickly coalesce to form a cavitation bubble and then collapse releasing a

significant amount of particles and mechanical energy, including acoustic wave, shock wave, and capillary wave. It is proposed that such energy may be sufficient to cause a secondary cavitation-based ablation of material from the target surface in water yielding to an explosion-like feature of craters, as shown in Figure 3.1 (a)-(c). For lower power intensities, no obvious formation of bubbles occurs. Thus, no such explosion-like character of the amorphous phase comes into being [Besner et al., 2005].

3.1.3. Calculation of Single Pulse Ablation Threshold and Laser Radius

Focus. Because the laser pulse in this experiment had a Gaussian distribution intensity profile, the development of the ablated crater areas should be consistent with the distribution given by equation (3.1).

$$E(r) = \int_{-\infty}^{\infty} I(r,t)dt = E_0 \exp(-2r^2 / \omega_0^2) \quad (3.1)$$

$$E_{pulse} = \int_0^{\infty} E(r)2\pi r dr = \int_0^{\infty} E_0 \exp(-2r^2 / \omega_0^2)2\pi r dr = \frac{\pi\omega_0^2 E_0}{2} \quad (3.2)$$

Using equation (3.2), the peak laser fluence E_0 could be varied by changing the pulse energy E_{pulse} or the laser dependent Gaussian beam radius ω_0 ($1/e^2$), as shown in equation (3.3).

$$E_0 = \frac{2E_{pulse}}{\pi\omega_0^2} \quad (3.3)$$

Equation (3.4) gives the empirical formula of the linear relationship between the diameters square of the surface damaged areas versus the logarithm of the laser pulse fluence [Tran et al., 2005]. E_{th} is the ablation fluence threshold.

$$d^2 = 4r^2 = 2\omega_0^2 (\ln E(r) - \ln E_{th}) \quad (3.4)$$

By extrapolating the linear line to horizontal axis, the threshold fluence can be obtained. Also, the laser focus radius ω_0 can be calculated from the slope of the plot. In order to get a good calculation result, some irregular ablation data points are eliminated. Figure 3.5 is the plot of the squared diameter versus the logarithm of the laser fluence. A linearly increasing relationship can be observed. The data is highly linearly distributed ($R^2=0.9876$). Using this technique, the ablation threshold for single pulse is calculated to be about 0.028mJ, which is close to the tested threshold value of 0.03mJ. Laser radius focus, also known as the beam waist, ω_0 , is calculated as $1.67\mu\text{m}$. It was verified that our laser was intensively focused by use of a 20X objective lens.

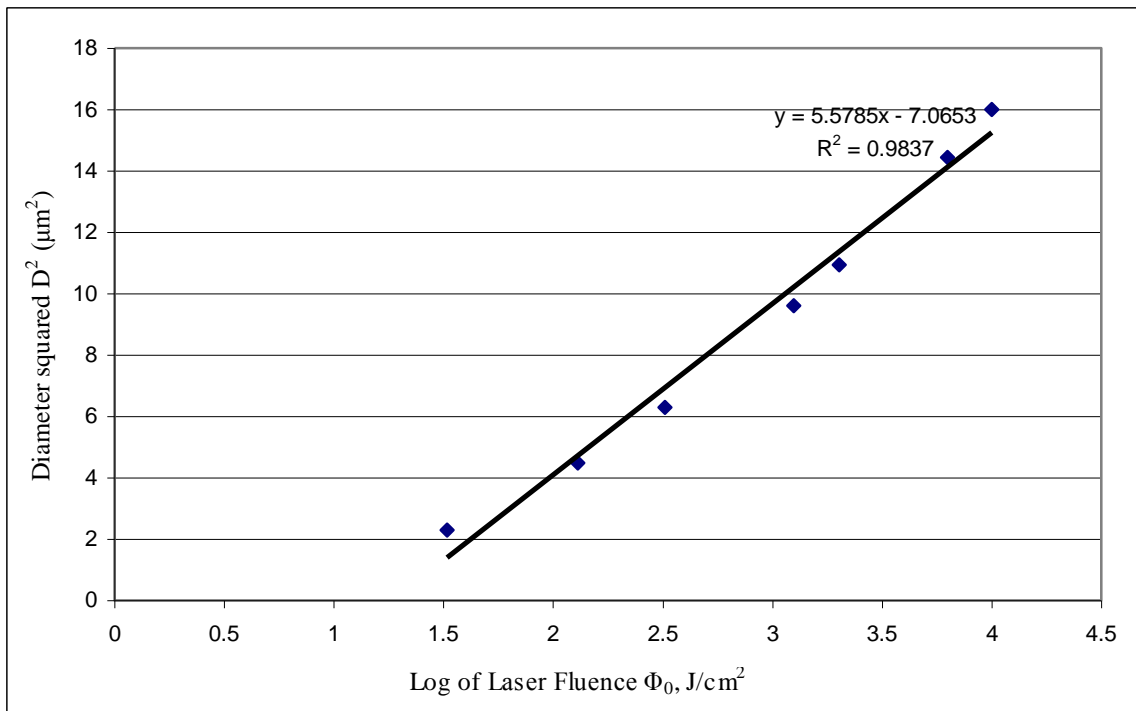


Figure 3.5. Square diameters versus laser energy ratio for treatment of silicon in water

3.2. EFFECT OF FOCAL POSITION

The position of the target surface with respect to the focal plane of the objective is the main variable in this section. The zero plane ($Z=0$) corresponds to the focal plane at the matter is surface, which is also at the beam waist. “+z” is defined as focal plane beneath the target surface, while “-z” is defined as focal plane above the target surface. The position of the focusing objective is shifted from $-60\mu\text{m}$ to $+60\mu\text{m}$ over the Z axis with an interval of $10\mu\text{m}$, as shown in Figure 3.6. The water layer is set to be 1 mm so that the target’s surface is always immersed in the liquid during the process. Laser power utilized in this case is 0.14mJ/pulse and single pulse ablation is applied. A detailed parameter description is listed in Table 3.2.

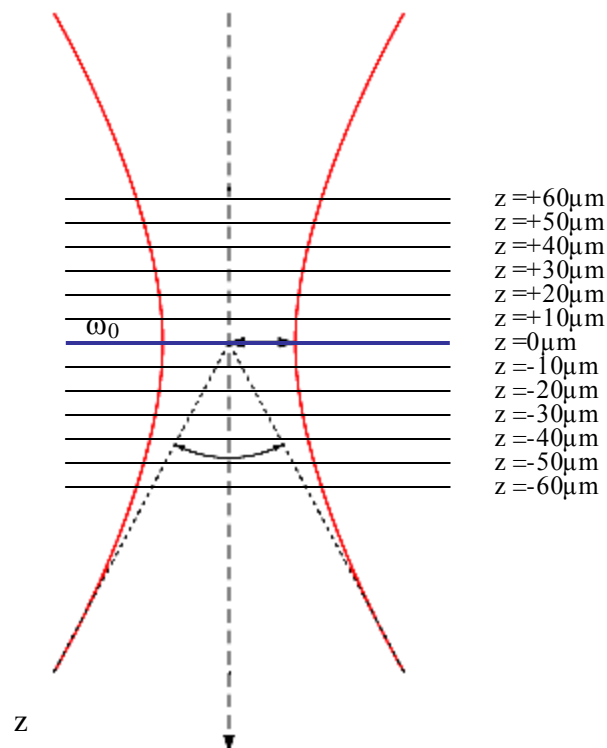


Figure 3.6. Schematic of focal position experiment setup

Table 3.2. Working parameters for focal position experiment in water

Laser power (mJ/pulse)	0.14
Pulse Number	1
Water Layer Thickness (mm)	0.8
Focal Position (μm)	-60, -50, -40, -30, -20, -10, 0, +10, +20, +30, +40, +50, +60
Objective Lens	20 X

Figure 3.7 and Figure 3.8 are SEM images of the surface morphologies after irradiation by a single laser pulse with different focal positions in the water and in the air, respectively. Images with the focal position of $\pm 60\mu\text{m}$ in water and $+60\mu\text{m}$ in air are not presented here because no visual surface damage was observed either via SEM or via the images obtained.

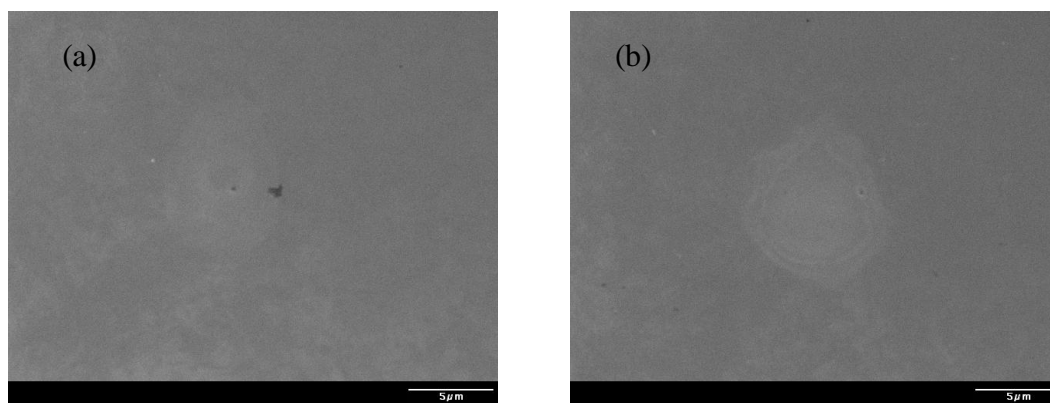


Figure 3.7. SEM images of surface morphologies after one laser pulse in water for the target position (a) $-50\mu\text{m}$, (b) $-40\mu\text{m}$, (c) $-30\mu\text{m}$, (d) $-20\mu\text{m}$, (e) $-10\mu\text{m}$, (f) $0\mu\text{m}$, (g) $+10\mu\text{m}$, (h) $+20\mu\text{m}$, (i) $+30\mu\text{m}$, (j) $+40\mu\text{m}$, (k) $+50\mu\text{m}$.

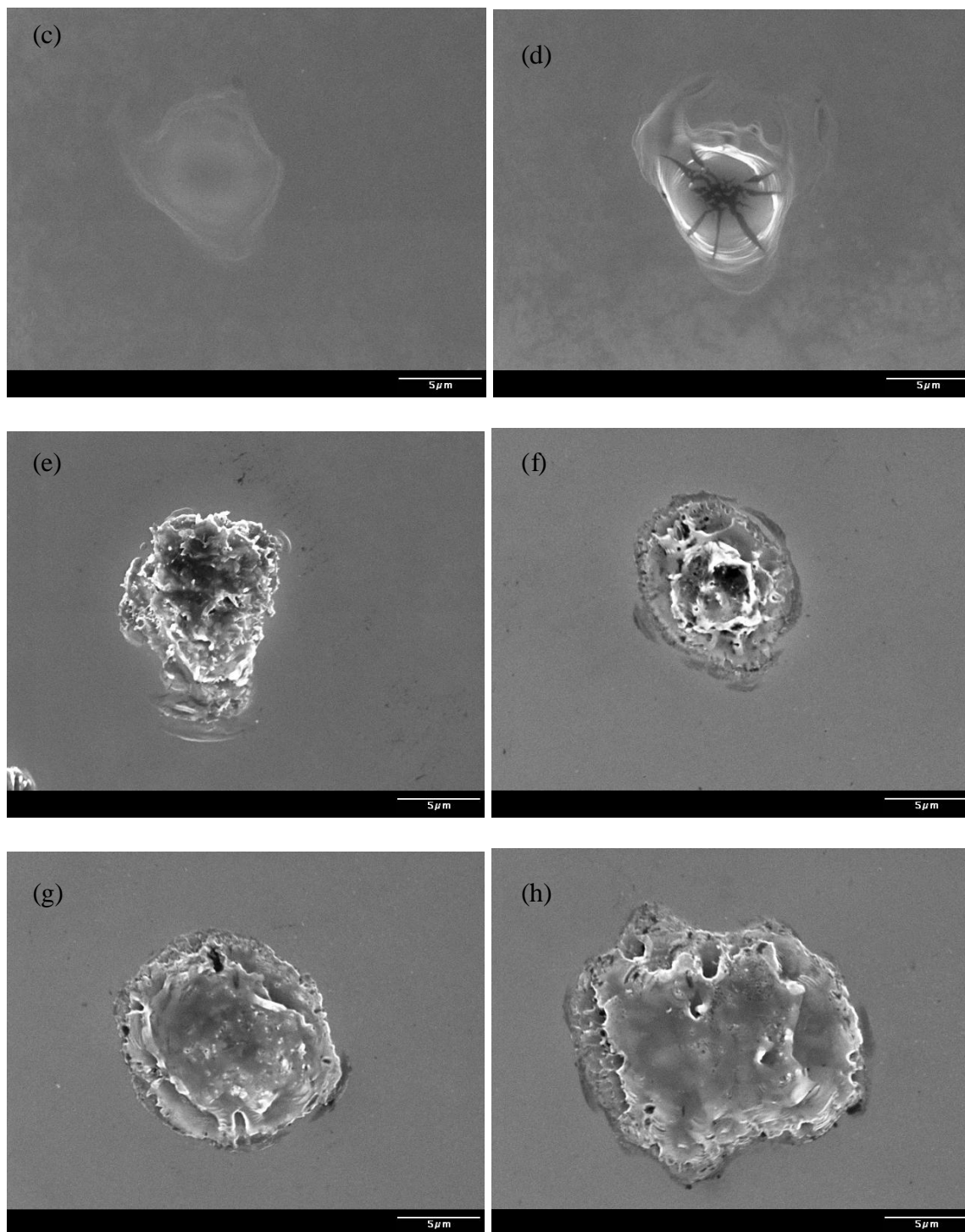


Figure 3.7. SEM images of surface morphologies after one laser pulse in water for the target position (a) $-50\mu\text{m}$, (b) $-40\mu\text{m}$, (c) $-30\mu\text{m}$, (d) $-20\mu\text{m}$, (e) $-10\mu\text{m}$, (f) $0\mu\text{m}$, (g) $+10\mu\text{m}$, (h) $+20\mu\text{m}$, (i) $+30\mu\text{m}$, (j) $+40\mu\text{m}$, (k) $+50\mu\text{m}$. (cont.)

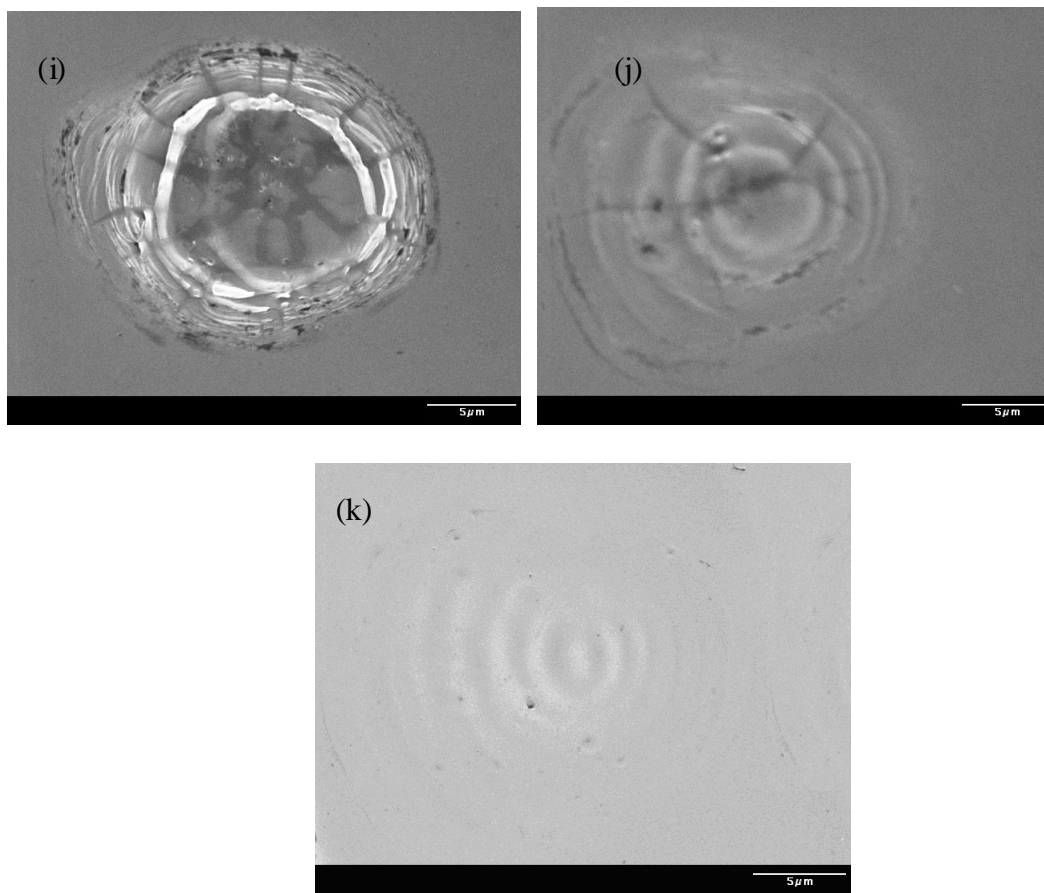


Figure 3.7. SEM images of surface morphologies after one laser pulse in water for the target position (a) $-50\mu\text{m}$, (b) $-40\mu\text{m}$, (c) $-30\mu\text{m}$, (d) $-20\mu\text{m}$, (e) $-10\mu\text{m}$, (f) $0\mu\text{m}$, (g) $+10\mu\text{m}$, (h) $+20\mu\text{m}$, (i) $+30\mu\text{m}$, (j) $+40\mu\text{m}$, (k) $+50\mu\text{m}$. (cont.)

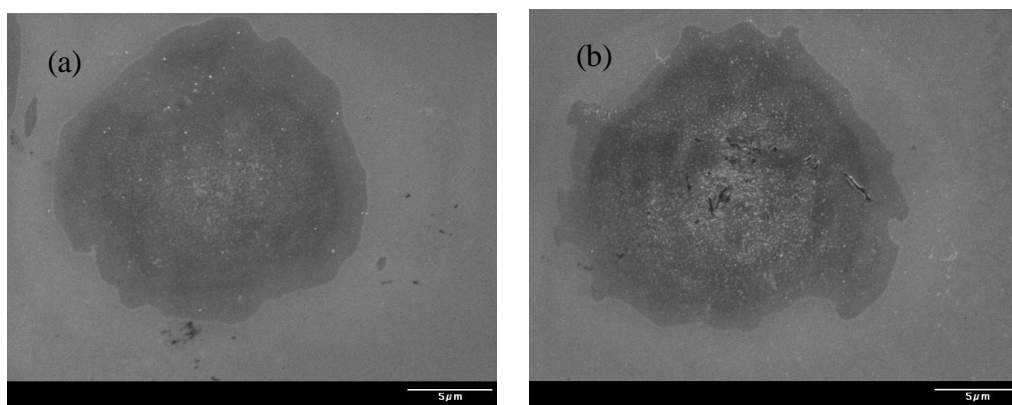


Figure 3.8. SEM images of surface morphologies after one laser pulse in air for the target position (a) $-60\mu\text{m}$, (b) $-50\mu\text{m}$, (c) $-40\mu\text{m}$, (d) $-30\mu\text{m}$, (e) $-20\mu\text{m}$, (f) $-10\mu\text{m}$, (g) $0\mu\text{m}$, (h) $+10\mu\text{m}$, (i) $+20\mu\text{m}$, (j) $+30\mu\text{m}$, (k) $+40\mu\text{m}$, (l) $+50\mu\text{m}$.

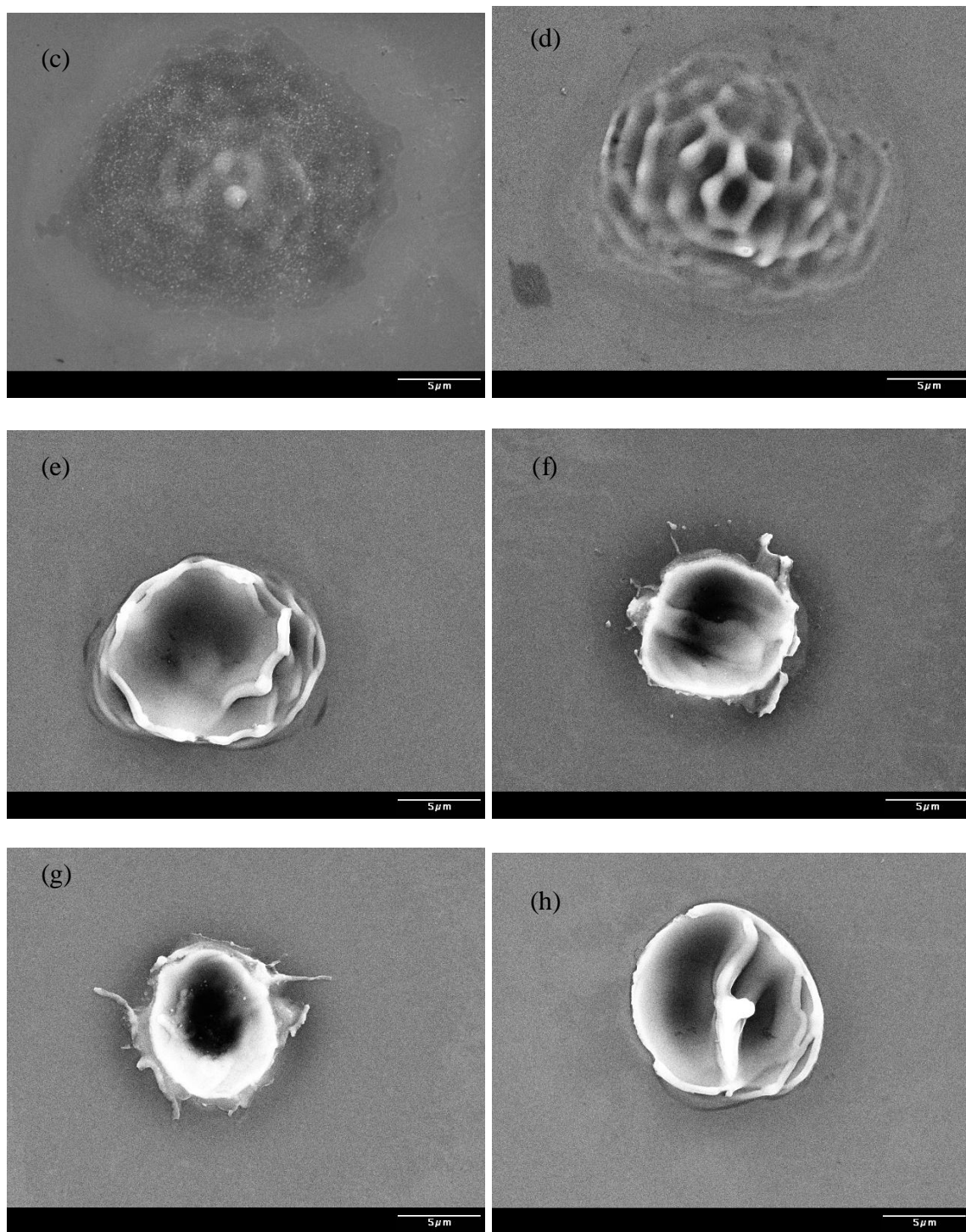


Figure 3.8. SEM images of surface morphologies after one laser pulse in air for the target position (a) $-60\mu\text{m}$, (b) $-50\mu\text{m}$, (c) $-40\mu\text{m}$, (d) $-30\mu\text{m}$, (e) $-20\mu\text{m}$, (f) $-10\mu\text{m}$, (g) $0\mu\text{m}$, (h) $+10\mu\text{m}$, (i) $+20\mu\text{m}$, (j) $+30\mu\text{m}$, (k) $+40\mu\text{m}$, (l) $+50\mu\text{m}$. (cont.)

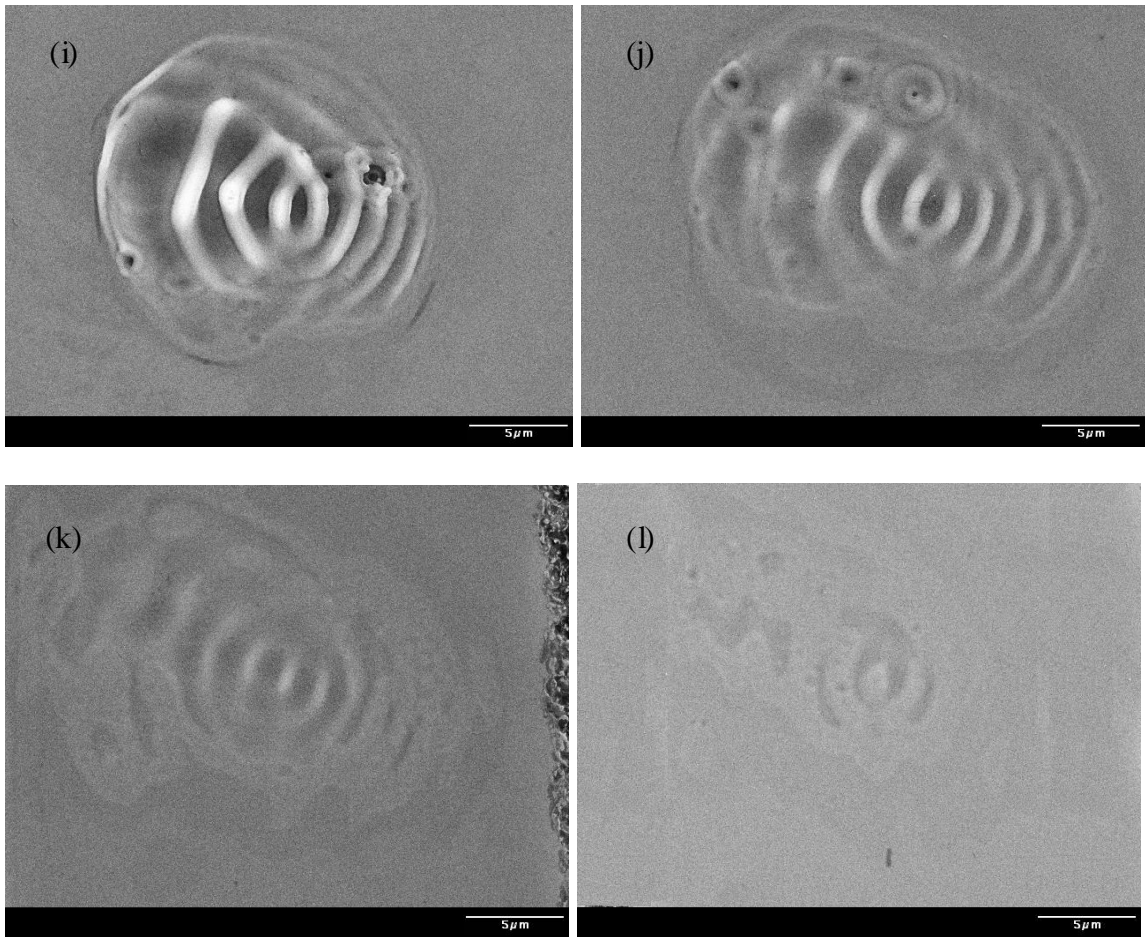


Figure 3.8. SEM images of surface morphologies after one laser pulse in air for the target position (a) $-60\mu\text{m}$, (b) $-50\mu\text{m}$, (c) $-40\mu\text{m}$, (d) $-30\mu\text{m}$, (e) $-20\mu\text{m}$, (f) $-10\mu\text{m}$, (g) $0\mu\text{m}$, (h) $+10\mu\text{m}$, (i) $+20\mu\text{m}$, (j) $+30\mu\text{m}$, (k) $+40\mu\text{m}$, (l) $+50\mu\text{m}$. (cont.)

According to Figure 3.7, as the focus plane shifts from $z=-60\mu\text{m}$ to $z=-30\mu\text{m}$, surface morphology changes from intactness into minor damage. Since the laser beam diverges extensively before irradiating on the target, not enough energy is deposited on the surface to cause severe ablation. No bubbles are developed to affect the laser-matter interaction process. A very thin layer of silicon is evaporated and removed immediately by water. Thus, only minor modification and a clean surface has been detected. At $z=-20\mu\text{m}$, sufficient energy is deposited onto the surface to form crater-like damage. At $z=$

-10 μm and 0 μm , rough, flower-shaped corrugation can be observed as shown in Figure 3.1 (a)-(c). Maximum energy is transferred to the surface as the beam waist comes closer. The plasma-bubble explosion mechanism explains the formation of this kind of amorphous morphology, as previously discussed. As the focus plane goes deep into the surface, the diameter of the ablation area increases because the spot size of the laser beam projected on the surface becomes larger. According to Figure 3.7 (g) and (h), the center of the modified area at $z=10\mu\text{m}$ to $30\mu\text{m}$ become a relatively flat and amorphous phase at the crater edge, which turned out to be less rough than $z=-10\mu\text{m}$ and 0 μm focal planes. Considering that less material was ablated and less plasma was induced, the size of bubble shrank correspondingly. The plasma-bubble explosion phenomenon has a weaker influence as the focal plane lowers. However, an interesting phenomenon occurs as the focal plane goes down to $z=+40\mu\text{m}$ to $+50\mu\text{m}$. A series of co-central ring-shape morphologies were found on the laser irradiated area. Since the laser beam waist is $+40\mu\text{m}$ to $+50\mu\text{m}$ underneath the material surface, it lead to violate molecular vibration. Unlike particles on the surface, particles in the bulk are confined by a large number of molecules. The highly stimulated molecules in a narrow region may release stress and kinetic energy like explosion in the form of shock waves in all directions. Since this phenomenon happens only 40~50 μm under the surface, the particles vibrate away from their original locations as the shock wave propagates to the surface without decaying to zero. As the surface waves freeze, the ring-shape morphology shown in Figure 3.8 comes into being. This mechanism is illustrated in Figure 3.9.

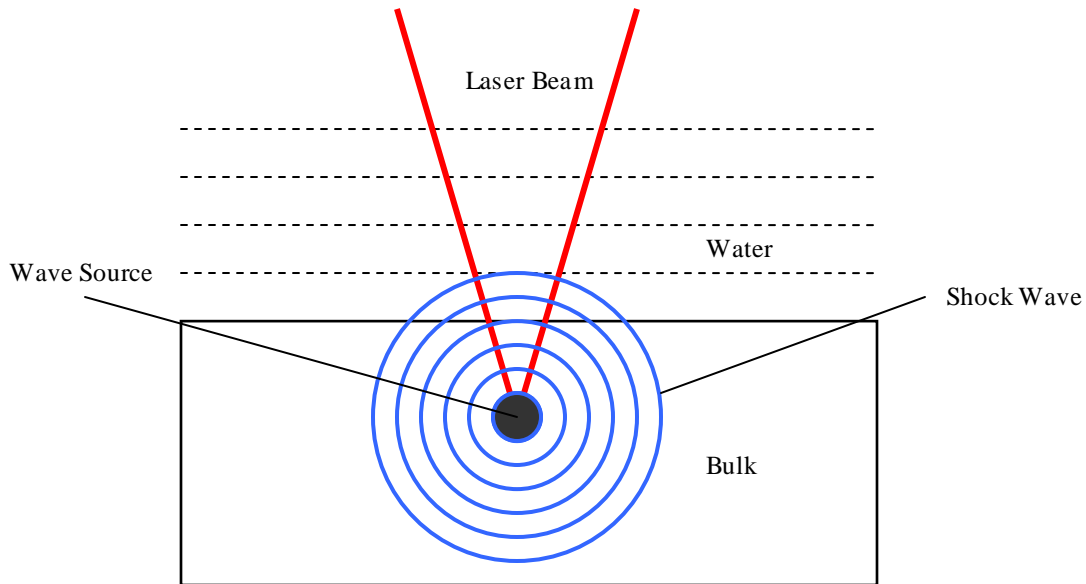


Figure 3.9. Shock wave propagation underneath the material surface

Similar co-center ring structures have been detected when the laser beam waist ranges from $z = +20\mu\text{m}$ to $z = +50\mu\text{m}$. The fact that ring structures appeared in both water and air verifies the explanation that shock wave propagation along the surface that induces the periodic rings. If the ring structures were caused by laser-water interaction or a plasma-bubble explosion, they could not form in air environment. When the focal plane shifted from $z = -10\mu\text{m}$ to $+20\mu\text{m}$, the same ablation process happened as discussed for Figure 3.2 (a)-(g). The surface morphology turned out to be two-region crater-like structures. As the beam waist was over $20\mu\text{m}$ above the target, energy deposited to the surface lowered down significantly. Three obvious phenomena occurred. First, the diameter of the modified region appeared to be larger than it was in water with the same focal position. This phenomenon is explained by the fact that the divergence of the beam in water is larger than in air. Laser energy diverges more severely in the water. When the

beam waist is above the target, the spot size in water is larger, but the effective beam area exceeding the damage threshold is less, the diameter of the damaged region in air appears to be much larger. Second, at $z = -60\mu\text{m}$ and $-50\mu\text{m}$, a thin layer of surface modification happened, but the surface is not as clean as in the water. Third, pits and corrugations started depositing severely on the target at $z = -40\mu\text{m}$ and $-30\mu\text{m}$ respectively. The pits may be caused by the silicon evaporation and re-deposit. These pits grow and become seeds of rough corrugations in the case of $z = -30\mu\text{m}$. The actual mechanism is still open to discussion.

3.3. EFFECT OF LASER PULSE NUMBER

This section examines how the morphology of the craters evolves with increasing number of laser shots under water. Laser energy used was 0.042mJ/pulse , which is slightly above the single-pulse ablation threshold. The interval between each shot was about 1 second so that the interference between individual pulses is minimized. All the other parameters are listed in Table 3.3.

Table 3.3. Working parameters for laser pulse number experiment in water

Laser power (mJ/pulse)	0.042
Pulse Number	1,5,10,50,100,250,500,1000
Water Layer Thickness (mm)	1.00
Focal Position (mm)	0 (right at the surface)

3.3.1. Ablation SEM Result Analysis. Figure 3.10 shows the surface evolution of ablation craters as the number of laser pulses, from 1 to 1000. As the number of pulses is increased, more material was removed from the center, so that the diameter and depth of ablation increased. According to SEM results, the crater morphology is discussed in two stages.

First of all, for 1 to 5 laser shots, the ablated areas had two distinct regions, a smooth but shallow crater and a protruding rim, like the morphology discussed previously in the low laser power ablation with single pulse experiment. The diameter of the crater caused by 5 pulses was arbitrarily larger than that induced by 1 pulse. However, in either case the energy was too low to cause obvious bubble formation. Thus, no pronounced plasma-bubble explosion effect occurred with a small number of pulse shots.

After 10 laser shots, the flower-like rough corrugation morphologies were detected around the center of the ablation spot. As the number of pulses went up, the energy transmitted to the silicon surface accumulated, which led to more plasma and larger bubble formations. The rough corrugation can be explained by the plasma-bubble explosion theory mentioned previously. When the pulse number increased from 250 to 500, the central ablated hole becomes deeper, obviously. However, from 500-1000, the diameters and depths of the craters do not vary much.

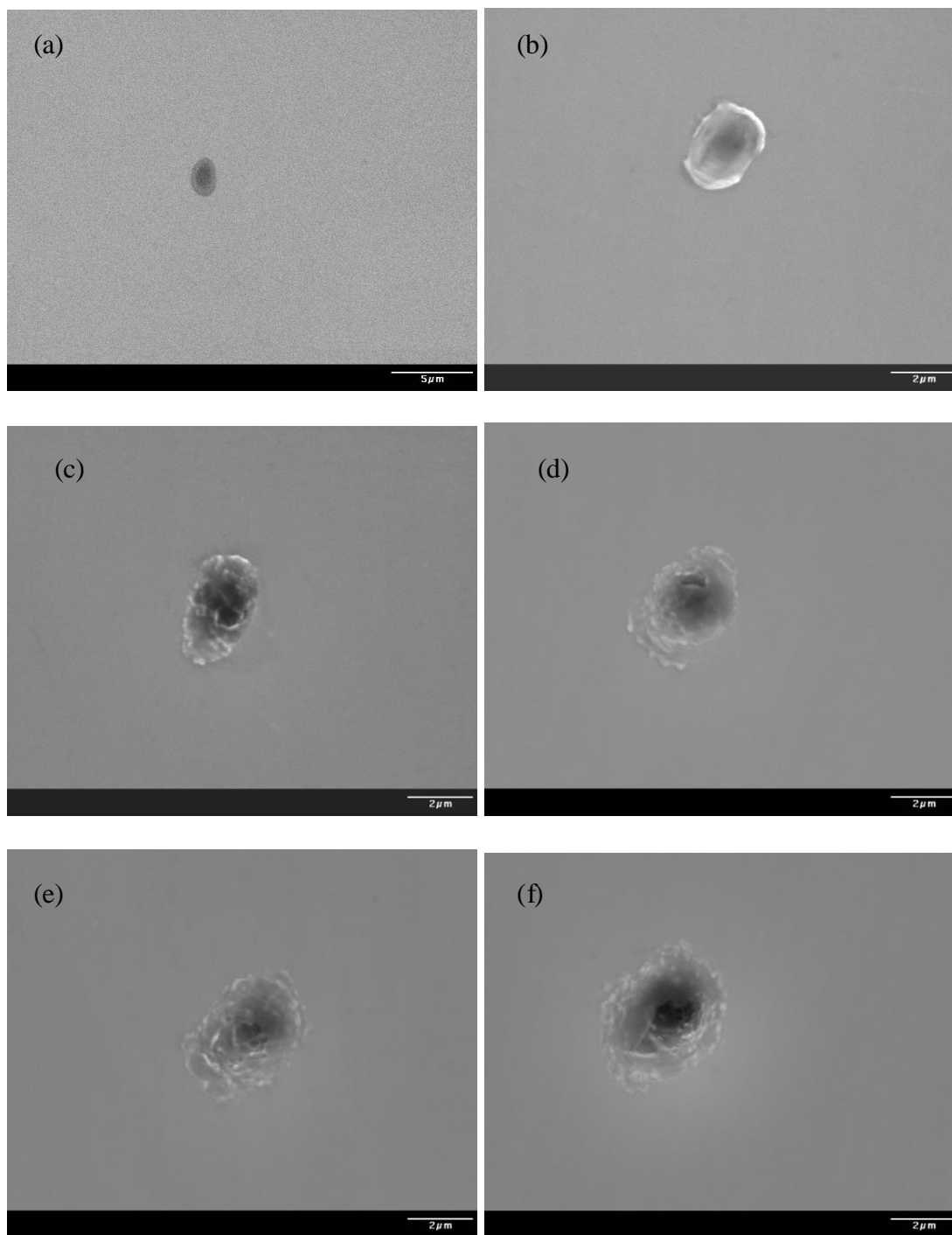


Figure 3.10. SEM images of ablation morphology at 0.042 mJ/pulse in water (a) 1, (b) 5, (c) 10, (d) 50, (e) 100, (f) 250, (g) 500, (h) 1000 laser pulses.

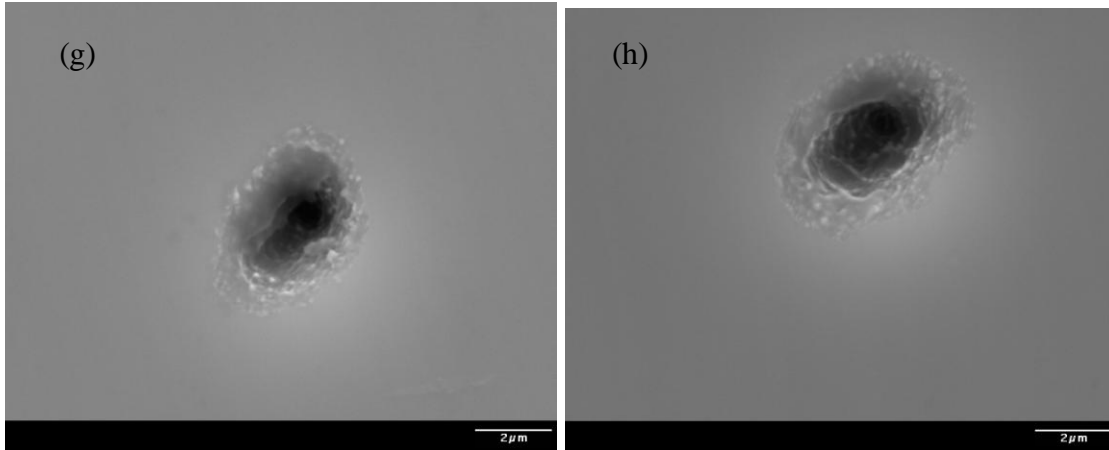


Figure 3.10. SEM images of ablation morphology at 0.042 mJ/pulse in water (a) 1, (b) 5, (c) 10, (d) 50, (e) 100, (f) 250, (g) 500, (h) 1000 laser pulses. (cont.)

By way of contrast, Figure 3.11 shows the ablation results obtained in air. The crater diameters and depths change significantly during the first 100 pulses, while remain almost the same after 100 shots. The surface corrugation at the edge of the rim is caused by silicon evaporation and re-deposit, and amorphous structure growth mechanism.

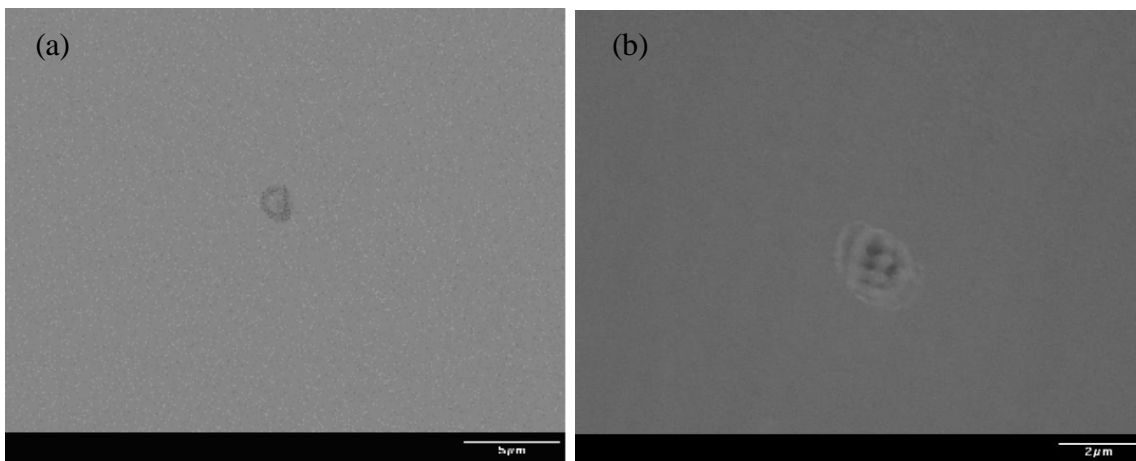


Figure 3.11. SEM images of ablation morphology at 0.042 mJ/pulse in air (a) 1, (b) 5, (c) 10, (d) 50, (e) 100, (f) 250, (g) 500, (h) 1000 laser pulses.

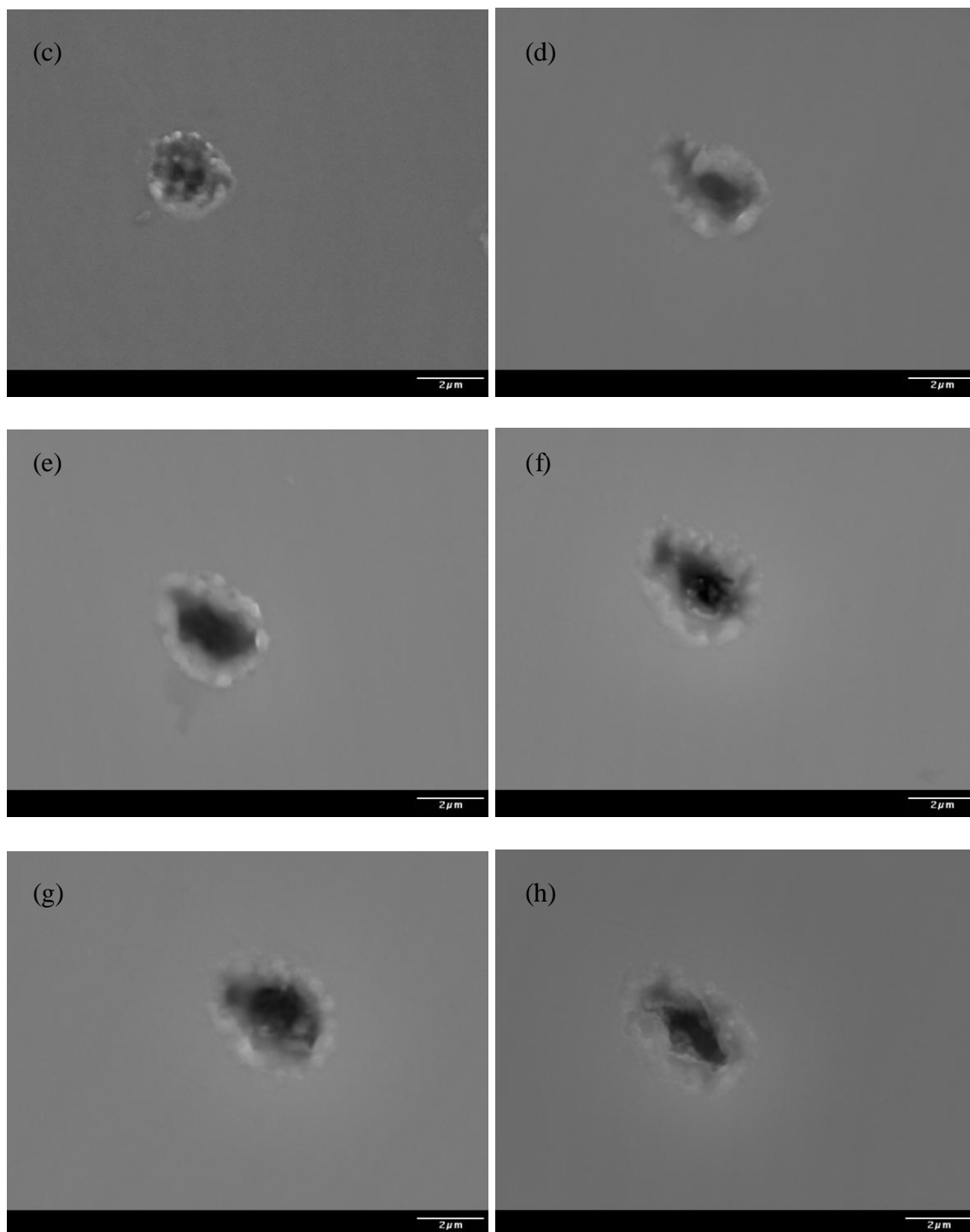


Figure 3.11. SEM images of ablation morphology at 0.042 mJ/pulse in air (a) 1, (b) 5, (c) 10, (d) 50, (e) 100, (f) 250, (g) 500, (h) 1000 laser pulses. (cont.)

3.3.2. Incubation Effect. Multi-pulse accumulation effects (incubation) have been known to lower the damage threshold of the materials [Jasapara et al., 2001]. The nature of the incubation is such that it affects the generation of the seed carriers on which avalanche ionization acts. The effective increase in the multi-photon absorption coefficients can be aroused due to the material modification caused by stress development, for example, due to defect formation and accumulation [Jasapara et al., 2001]. When the pulse number is small, the impurities and defects occur in the crystalline lattice for ablation. As it becomes larger, the defects and impurities are the seeds for avalanche ionization. While this accumulation process develops, the depth of the crater deepens and its diameter increases. However, according to most of the research about the incubation effect, the diameter and depth change sharply at the first few pulses, then, as the ionization reaches a limit, the diameter and depth vary insignificantly [Baudach et al., 1999; Kirkwood et al., 2005; Coyne et al., 2004].

From theoretical study about the incubation model, an empirical formula (equation (3.5)) has been given to relate the crater diameters, D , to the laser shot number, N .

$$D = \omega_0 \sqrt{2 \ln \left(\frac{\phi_0}{\phi_{th} (1) N^{S-1}} \right)} \quad (3.5)$$

ω_0 – Diameter of Gaussian beam waist

Φ_0 – Laser fluence per one pulse

Φ_{th} – Ablation threshold fluence for a single pulse

S – Incubation parameter

When changing the equation (3.5) into the form of equation (3.6), the squared diameter is easily found to be linear with response to the logarithm of the pulse number.

$$\frac{D^2}{\omega_0^2} = 2 \ln \frac{\phi_0}{\phi_{th}(1)} - 2(S-1) \ln(N) \quad (3.6)$$

Figure 3.12 shows the experimental data for diameters of the ablated holes obtained in 3.3.1. Two solid lines represent least-square fits. According to the previous calculation $\omega_0=1.67\mu\text{m}$, the incubation parameter can be found by the slope of the lines. The incubation parameters are 0.060 and 0.377 respectively for water and air. According to incubation theory, the larger the S, the less the incubation effect takes place. When $S=1$, incubation is absent. Thus, it can be concluded that the incubation effect in water is much more pronounced in water than in air. So far, the incubation effect of multi-pulse irradiation and its more pronounced effect in water than in air are still open to discussion.

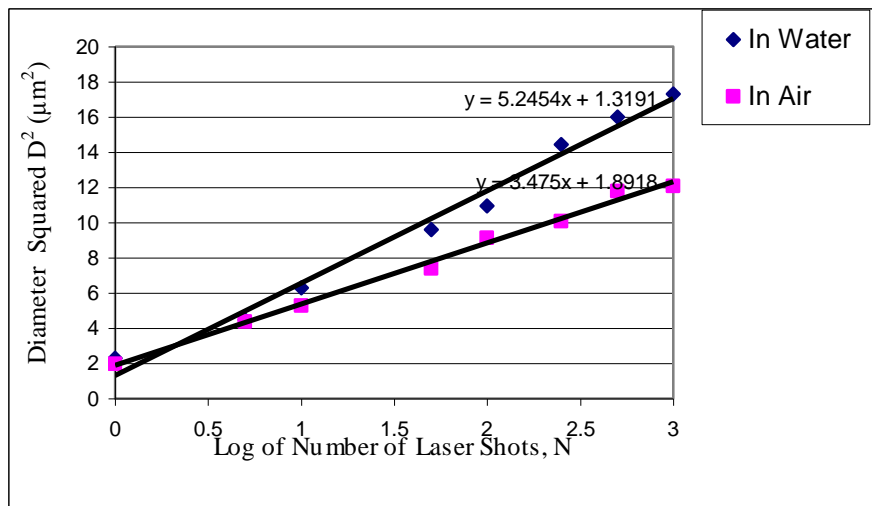


Figure 3.12. Graph of diameter squared as a function of log of the laser pulse number of 1, 5, 10, 50, 100, 250, 500, 1000, respectively, both in the water and the air.

3.4. SUMMARY OF LASER ABLATION IN THE WATER

First of all, for both water and air, the tested laser ablation threshold for single pulse shot was 0.03mJ. With increasing laser power, the crater-shaped structure appears with two distinct regions: the central damage is caused by laser-induced material removal, while the outer rim forms by amorphous re-deposition. As the laser power reached a very high level, the two region crater remained the same shape for ablation in the air. However, for ablation in the water, the morphology evolves into flower-like corrugations, which are caused by bubble-explosion induced waves and surface waves' interaction effect. A linear relationship between the diameters square of the craters versus the logarithm of the laser pulse fluence has been obtained and the theoretical single pulse ablation threshold and laser focal radius have been calculated.

Ablation with focal positions below the surface lead to a sequence of co-central rings appearing both in the water and in the air. The laser-induced material breakdown started from the inner bulk and the shock waves propagated in all directions. The surface atoms moved away from their equilibrium locations and periodic ring-shape waves formed. As the focal position moved towards the surface, flower-like rough corrugations came out for ablation in water and two-region craters came out for ablation in the air. As the focal position moved above the surface, flower-like corrugations and two-regional craters diminished gradually both in the water and in the air.

As the number of laser pulses increased, the diameter and the depth of the laser-induced craters increased. A linear relationship of diameter squared versus the logarithm of the laser pulse number has been derived. The incubation effect theory is applied to illustrate the energy accumulation process of multi-pulse of ablation.

4. FEMTOSECOND LASER-INDUCED SURFACE MORPHOLOGY IN WATER

Micro-structuring by using femtosecond laser has been widely discussed as a promising technique for total analysis system (μ -TAS) fabrication. The femtosecond laser direct-write process is controllable by programming and is highly efficient. However, femtosecond induced micro/nano-scale periodic structures make the product surface too rough to be acceptable in the industrial world. Femtosecond laser direct-write sub-micron structures such as channels and resonators have been reported on transparent material like glass [Dong et al., 2003; Hwang et al., 2004]. Because these surfaces were still not acceptable, chemical etching was suggested as a methodology to remove surface roughness [Dong et al., 2003]. Although it works for specific kinds of materials in special solutions, it is not effective in every single case. Etching also lowers the fabrication efficiency. Thus, it is still worthwhile to look for a proper set of parameters for fabricating a smooth surface with a femtosecond laser. Especially for Si, the most common dielectric material in use, the ultra-fast pulsed laser induced periodic structure is phenomenal, which makes it difficult to achieve a satisfactory surface after laser irradiation.

The previous chapter reviewed a fundamental research on femtosecond laser induced one-pulse and multi-pulse ablation, revealing the basic physics behind laser-matter interaction process. This chapter discusses some unique results of a laser direct-write experiment which hold promise in the field of femtosecond laser application in Si micro/nano-machining.

4.1. EFFECT OF REPETITION RATE

The repetition rate largely influences the deposited energy, laser overlapping, and laser-surface wave interference state on the surface of silicon. In this section of the experiment, a $200\mu\text{m}$ by $150\mu\text{m}$ rectangular pit was fabricated by direct laser writing. A laser beam scanned back and forth at a constant velocity so that femtosecond laser incidentally and evenly irradiates onto the surface, as shown in Figure 4.1. The distance between each scanning line is set to $1\mu\text{m}$ in order to get a good overlapping of each adjacent scan. The whole pit was shaped after repetitively scanning three layers in the same way.

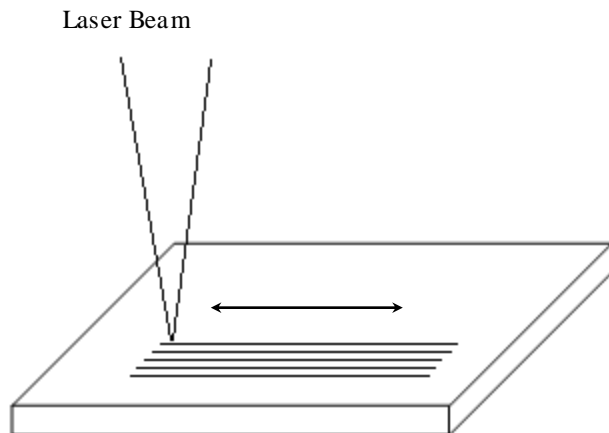


Figure 4.1. Femtosecond laser surface scanning tracks

Table 4.1 lists all the detailed parameters used in laser repetition rate experiment. The shutter was able to control the repetition rate change from 1 to 500Hz. Six typical frequencies were selected in this experiment so as to fully elucidate the evolution of the

surface patterns with the repetition rate. The traveling speed of the stage was controllable. Here, it was set as 3mm/min. Then it was calculated that the overlapping were 10 pulse/ μm , 6.6 pulse/ μm , 5 pulse/ μm , 3.2 pulse/ μm , 2 pulse/ μm and 0.2 pulse/ μm for 500Hz, 333Hz, 250Hz, 167Hz, 100Hz, and 10Hz respectively. All the experiments were taken in water confinement.

Table 4.1. Working parameter list for laser repetition experiment in water

Repetition Rate (Hz)	500, 333, 250, 167, 100, 10
Laser Energy (mJ/pulse)	0.14
Scanning Speed (mm/min)	3
Water Layer Thickness (mm)	3.00
Focal Position (mm)	0 (right at the surface)
Objective Lens	10 X

4.1.1. SEM Analysis and Mechanism Discussion. The damaged surfaces after femtosecond laser scanning with different frequencies are shown in Figure 4.2. All the images were taken at the same scale. The surface pattern after irradiation was found to vary significantly with the repetition rate when the scanning speed was fixed.

For 500Hz, with the laser overlapping of 10 pulse/ μm , the surface looked very corrugated. Irregular boulder-like bumps between 3 μm to 10 μm protruded above the basis with numerous nano-particles deposited on the surface of the bumps. For 333Hz

(6.6 pulse/ μm), the surface turned out to be flatter than that of 500Hz. However, there still existed furrow-like grooves. When the repetition rate was lowered down to 250Hz and 167Hz (5 pulse/ μm and 3.2 pulse/ μm), deep grooves were not phenomenal. Some 1 or 2 micron deep pits and the same scale bumps dominated the surface roughness. For 100 Hz (0.2 pulse/ μm), one interesting phenomenon was that the surface becomes extraordinarily smooth compared to other frequencies. Nano-particles and some local roughness were detected. For 10Hz, parallel ridge-like structures were found protruding out of the surface. The distance between the ridges was about $1\mu\text{m}$, while the heights were less than $2\mu\text{m}$. According to the above laser scanning results, a repetition rate of around 100Hz, with a laser overlapping of 2 pulse/ μm , are good parameters for obtaining a smooth surface for application requirement.

Interestingly, although the same overlapping would be obtained by fixing the repetition rate and changing scanning speeds, surface roughness did not change obviously as that by changing repetition rate. For example, when the repetition rate was set to 1000Hz, we did not find smooth surface when the traveling speed was 6 mm/min.

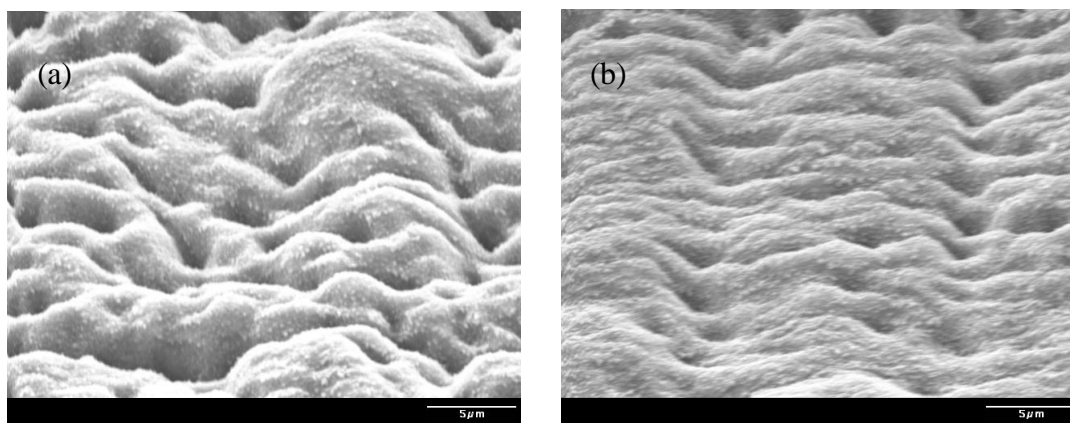


Figure 4.2. SEM images of femtosecond laser-induced surface morphology in water (a) 500 Hz, (b) 333 Hz, (c) 250 Hz, (d) 167 Hz, (e) 100 Hz and (f) 10 Hz.

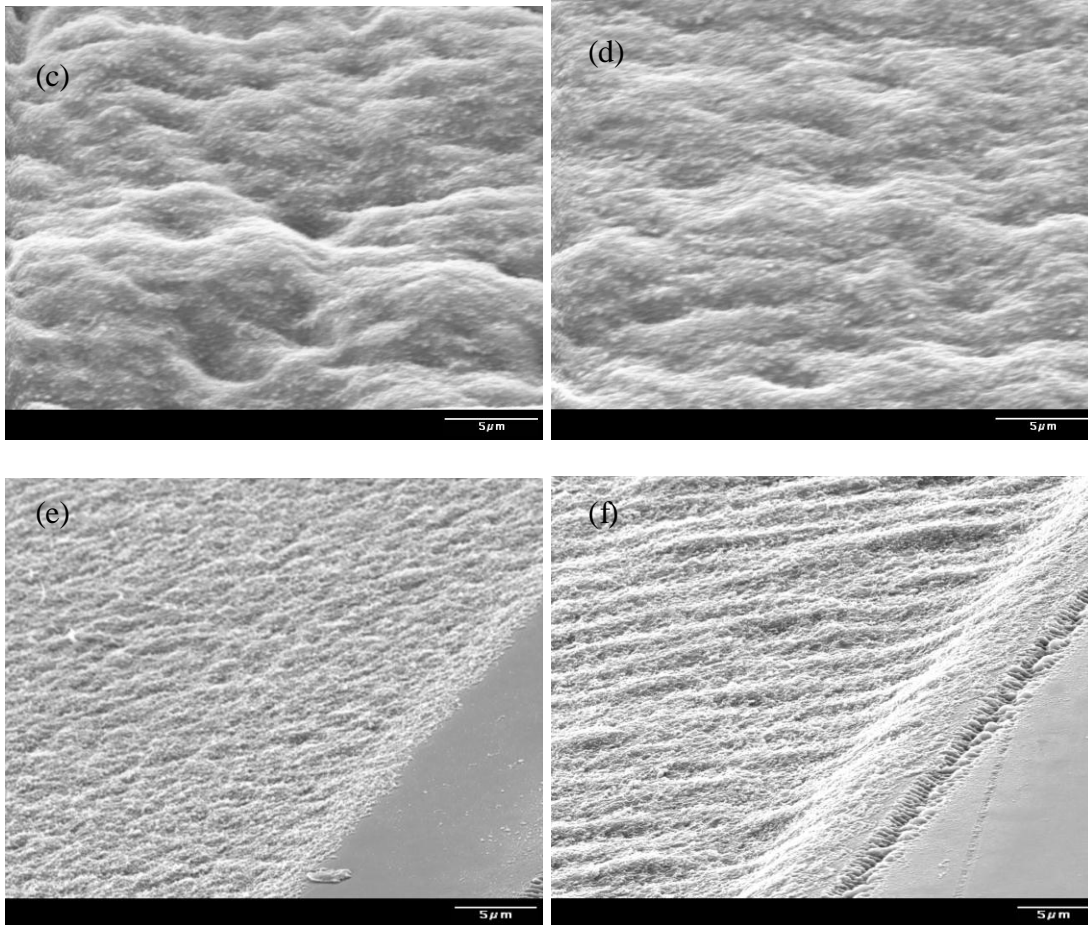


Figure 4.2. SEM images of femtosecond laser-induced surface morphology in water (a) 500 Hz, (b) 333 Hz, (c) 250 Hz, (d) 167 Hz, (e) 100 Hz and (f) 10 Hz. (cont.)

By way of contrast, identical experiments were conducted in the air with the same series of parameters. The phenomenal laser-induced periodic cones came into being, as shown in Figure 4.3. The diameter of the cones was the scale of 1-2 μm as the repetition rate changes from 500Hz to 100Hz, but the height of the cones for 100Hz was prominently smaller than that for 200Hz. As the frequency lowered down to 10Hz, the laser overlapping is 0.2 pulse/ μm , so only one laser pulse was incident to the surface per 5 μm . Considering the laser focal beam size is about 2 μm , the laser overlapping effect in

this case is therefore very poor for forming an entire region of patterns. Correspondingly, only discrete ripples form unevenly on the material surface.

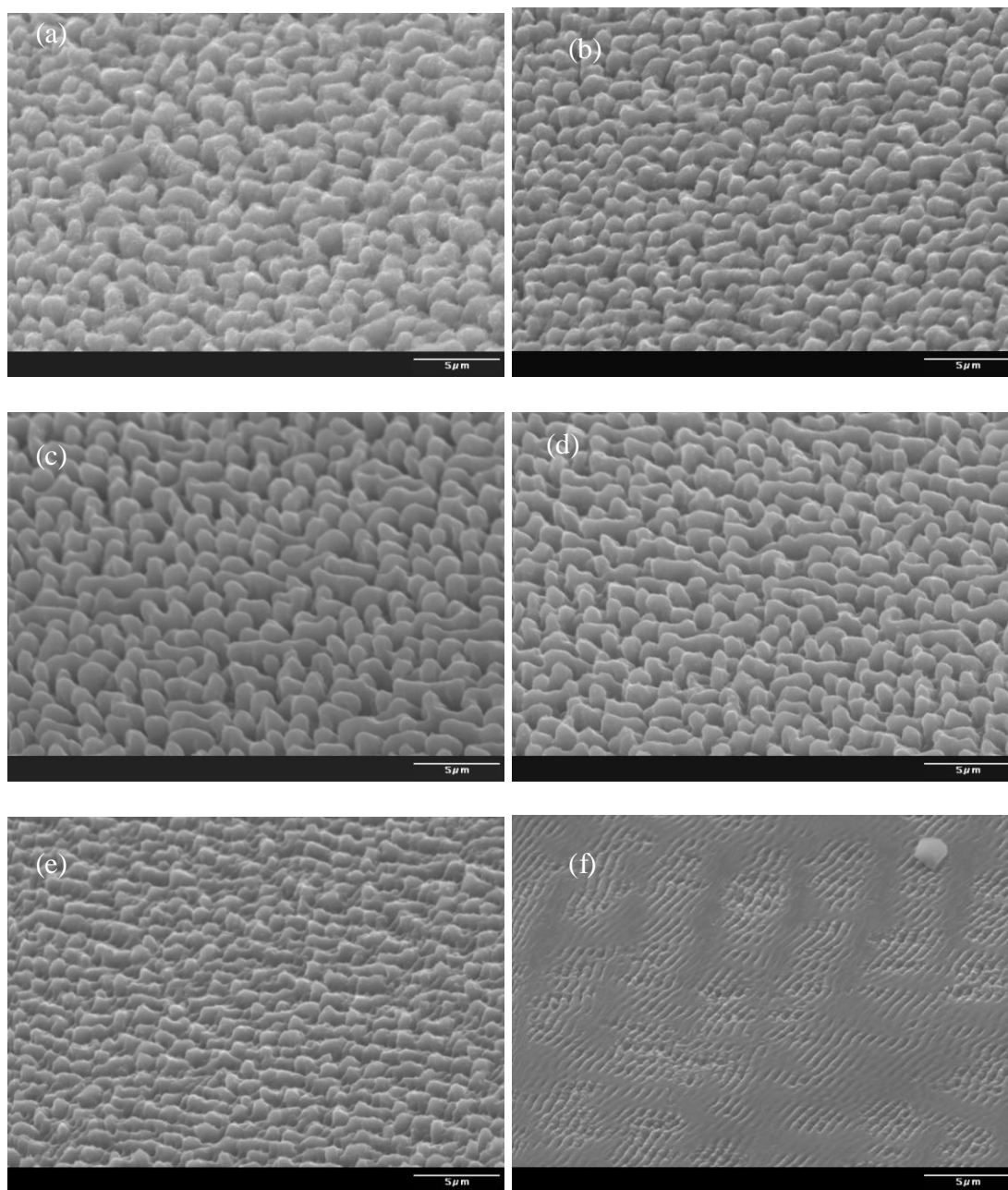


Figure 4.3. SEM images of femtosecond laser-induced surface morphology in the air (a) 500 Hz, (b) 333 Hz, (c) 250 Hz, (d) 167 Hz, (e) 100 Hz and (f) 10 Hz

The potential mechanism of laser induced periodic structure formation in the air has been widely discussed. The EDS analysis of a surface irradiated by laser in the air, shown in Figure 4.4, indicates that oxidation might be a reason for the formation of nano-particles on the columnar spikes [Seifert et al., 2005], since the content of oxygen is much higher than that in the water. Figure 4.5 shows the EDS results of a silicon surface ablated in the water. The most widely accepted explanation takes into account the interaction of an electromagnetic wave with the microscopically rough selvedge of the surface. As the laser light hits onto the surface, the light may be refracted by the material, as well as scattered by the selvedge. The incoming laser light then interferes with the surface waves, leading to periodic electromagnetic field distribution. Hence, periodic structures form on the material surface [Georgescu et al., 2006].

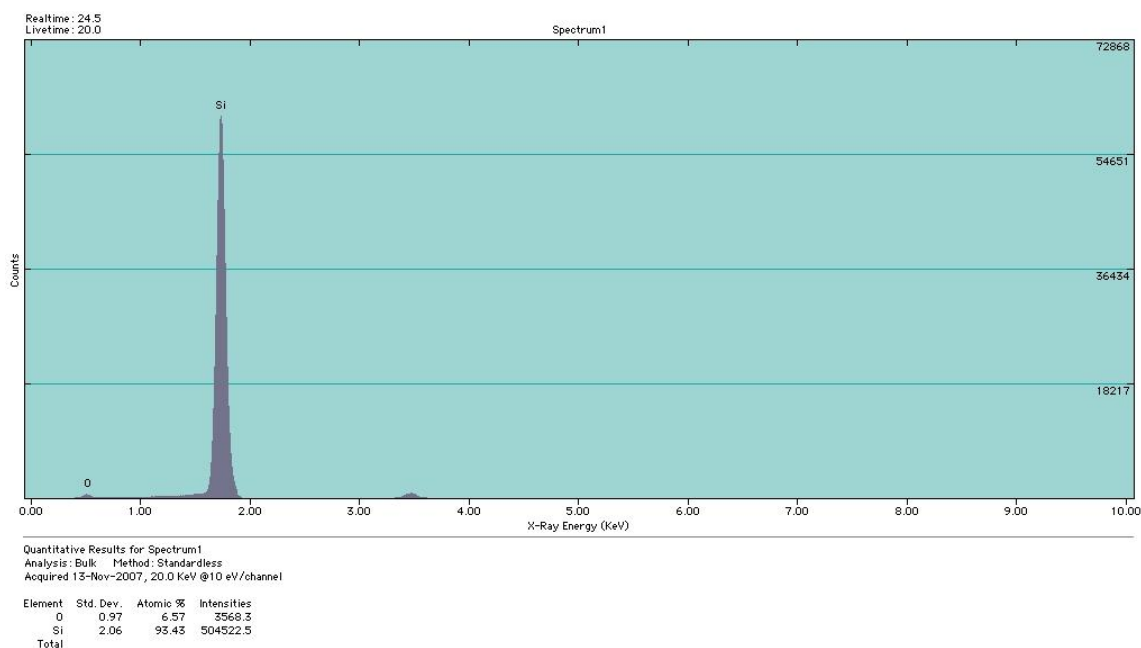


Figure 4.4. EDS analysis of silicon surface processed in the air

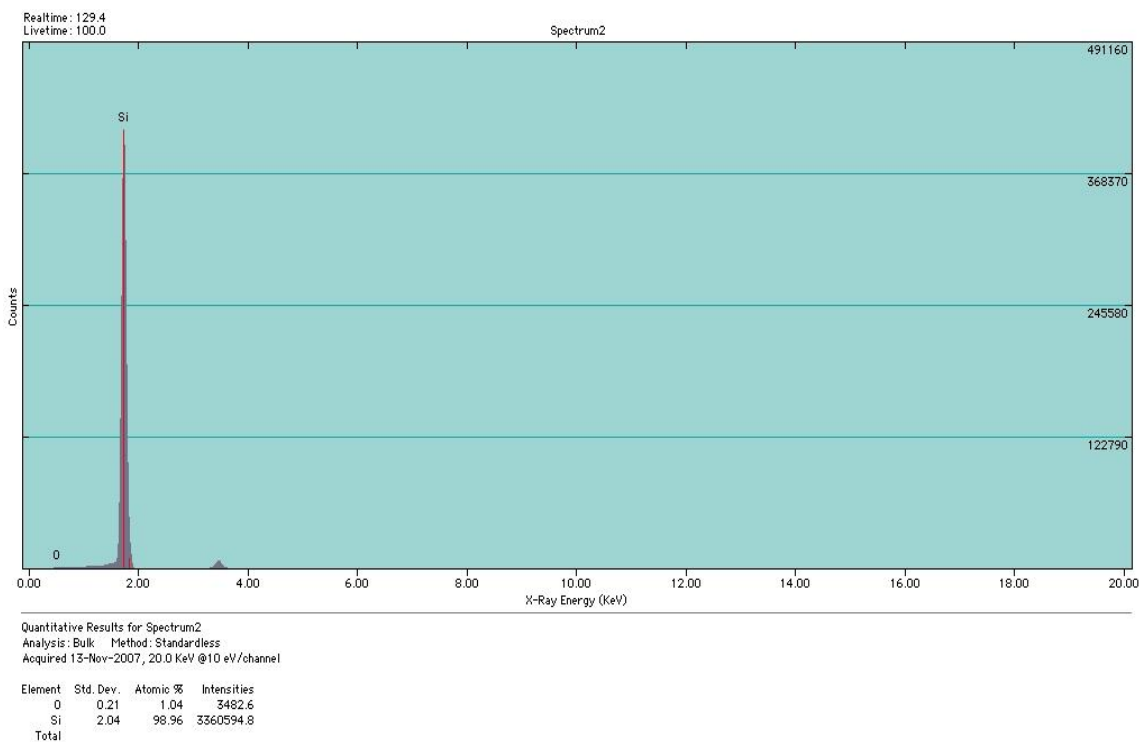


Figure 4.5. EDS analysis of silicon surface processed in the water

The formation mechanism of surface pattern by laser direct writing in the water has seldom been studied. For underwater laser scanning, incident laser light interference with the surface waves is a possible reason for the boulder-furrow-like structure formation at frequencies of 167Hz to 500Hz. However, the morphology is not as regularly periodic as that obtained in the air. The water layer plays the role of shielding source from laser energy. The absorption coefficient in water is 3/m, as shown in Figure 4.6. With a 3 mm water layer, only 0.9% of laser energy was absorbed. Thus, absorption should not be regarded as a main reason for the special structure formation on the surface.

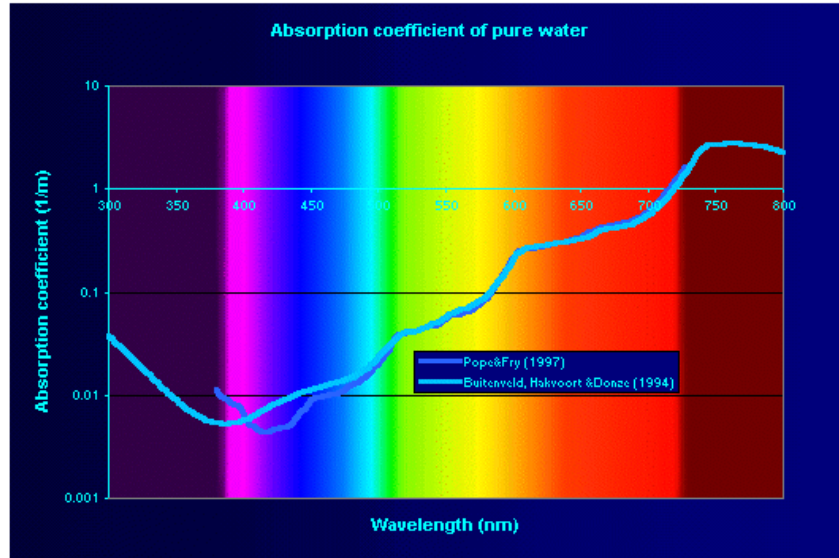


Figure 4.6. Absorption coefficient of water versus wavelength [www.deeptune.net]

Two possible causes of the special surface patterning phenomenon in water. First, as discussed in the previous chapter, the interference processes are significantly impacted by the cavitation bubbles caused by plasma formation and water evaporation. This might be a reasonable explanation for why the surface is corrugated, but not as regular as that in the air. Another reason is that H_2O molecules are strongly polarized due to the high electronegativity of the O atoms. During the scanning process, the laser beam can be considered as a moving electromagnetic field on the sample surface. This moving electromagnetic field will affect the energy status of H_2O molecule because of its polarization. Then it influences the electromagnetic field itself in return.

The ripple-like surface pattern appears on the surface at laser overlapping of 0.2 pulse/ μm because the laser overlapping is too poor to ensure sufficient energy irradiation onto the entire area. The bubbles scatter the incident light and change the interaction of laser light with surface waves. Hence, periodic ridges that look very

different from the structures formed in the air develop a repetition rate of 100 Hz, with a laser overlapping of 2 pulse/ μm , the surface roughness is almost at a minimum level. Profound numerical and physics investigations of the surface smoothing mechanism at 100 Hz need to be conducted to develop an understanding of the mechanism of laser and material interaction at the water-material interface.

4.1.2. AFM Analysis and Applicability. A 3D representation, AFM analysis has been conducted to further examine the surface roughness and observe the fine surface structures created by 100Hz femtosecond laser direct-write in water. Figure 4.7 shows a picture of a square ($5 \times 5 \mu\text{m}^2$) surface region. It demonstrates the topology and height difference between the maximum and minimum under $2 \mu\text{m}$. The averaged surface roughness on vertical level is about $1.5 \mu\text{m}$. Tiny bumps of about 100~200nm have also been found on the surface. Obviously, these nano-size bumps are not caused by re-deposition as they are in the air, because water removes the debris immediately from the surface and suspends it in the water. The exact mechanism of these nano-size particles requires further study. Although the AFM analysis did not show a shocking roughness result, the surface quality obtained at this repetition rate is much higher than at other repetition rates, both in water and in air. In those cases, surface roughness is out of the AFM measurement range.

Figure 4.8 (a) and (b) show V-shape grooves fabricated in the air and in the water, respectively. The dimension of the groove is $50 \mu\text{m}$ at width by $25 \mu\text{m}$ at depth. In the light of previous experiment results, the laser repetition rate of 100 Hz was applied to get a better surface quality. It can be seen that a much smoother groove surface and sharper angle have been obtained through manufacturing in water confinement. In the air,

periodic structures dominate the surface, thereby making surface too rough to be a usable product.

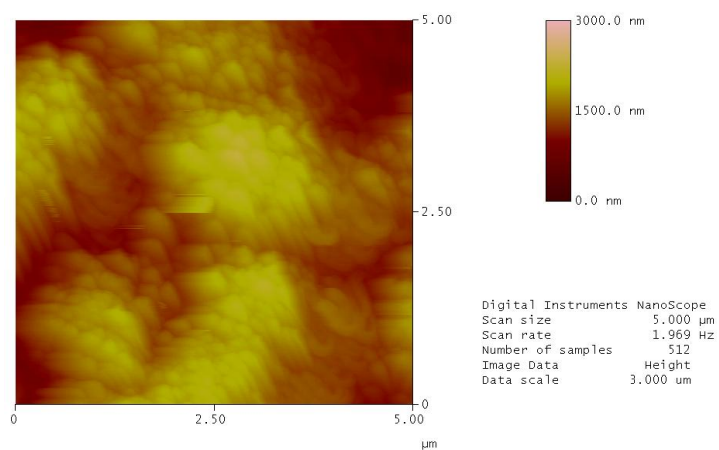


Figure 4.7. AFM picture of the surface irradiated by 0.14 mJ/pulse femtosecond laser at 100 Hz in water confinement

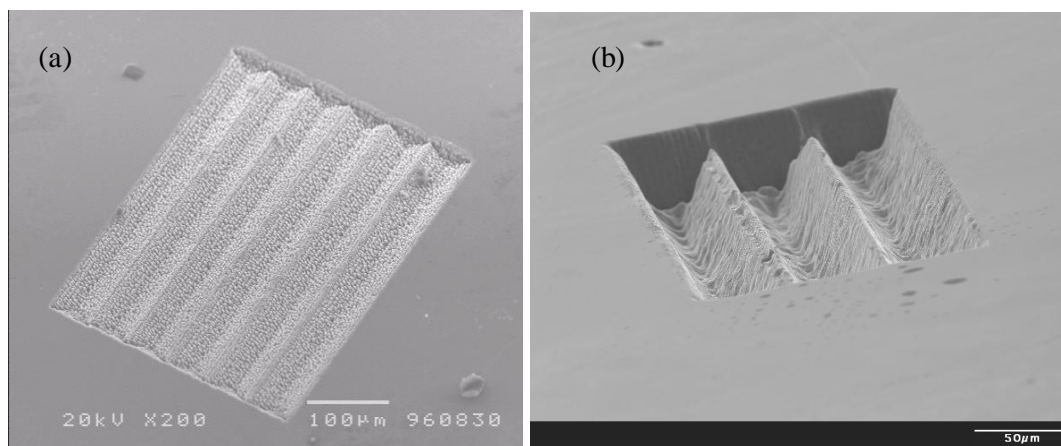


Figure 4.8. V-shape grooves fabricated by fs laser direct writing (a) in air, (b) in water

4.2. EFFECT OF LASER POWER

Apart from laser repetition rate, laser power is another factor that largely influences the energy deposited on the surface in the laser scanning process. In this section, six different laser powers ranging from a low power, just above the ablation threshold to a higher power, which induces obviously deep penetration, were applied. The repetition rate was fixed at 100 Hz and scanning speed is set as 3 mm/min. This combination yields a laser overlapping of 2 pulse/ μm , the characteristic value determined for good surface quality. Detailed experiment parameters are listed in Table 4.2. All the experiments were conducted in water. Another group of experiments were conducted in the air with the same working parameters.

Table 4.2. Working parameter list for laser power experiment in water

Laser Energy (mJ/pulse)	0.06; 0.16; 0.5; 1; 2; 3
Repetition Rate (Hz)	100
Scanning Speed (mm/min)	3
Water Layer Thickness (mm)	3.00
Focal Position (mm)	0 (right at the surface)
Objective Lens	10 X

As laser energy increases from 0.06 mJ/pulse to 3 mJ/pulse, the surface structure evolved as is shown in Figure 4.9. For 0.06 mJ/pulse, the surface remained almost

undamaged, with only some local roughness. The incident laser intensity was too low to strongly interfere with surface tensions. When the laser energy per unit pulse rose up to 0.16mJ, rough bumps were found protruding unevenly on the surface. Worm-like ripples developed as the laser power increased to 0.5 mJ/pulse. The structures were more regular in comparison than other images and looked similar to those in Figure 4.2 (a) and (b). As previously discussed, this kind of morphology is caused by multi-interference among incident laser lights, refractive waves, and bubble-induced mechanical waves. For this energy and frequency combination, standing waves formed on the surface so that regular ripples came out. As the energy reached 1.0mJ/pulse, the edges of the ripples became very blurry and the tips turned out to be blunt. An intensive incident laser power induced a stronger electromagnetic field, which altered the surface wave oscillation status, as in the 0.5mJ/pulse case. For higher energy, as are shown in the Figure 4.9 (e) and (f), the surface morphology is obviously different.

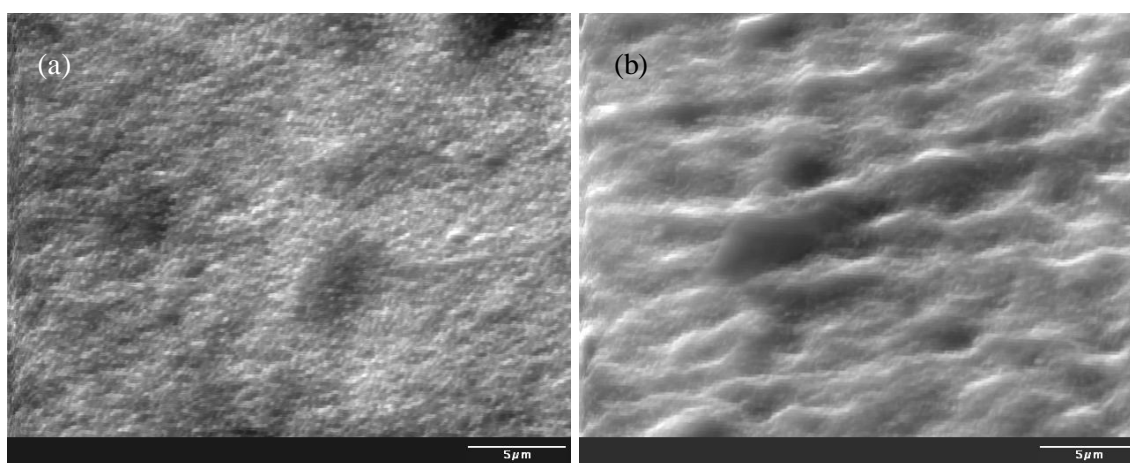


Figure 4.9. SEM images surface pattern formed in water by laser energy (a) 0.06mJ/pulse; (b) 0.16mJ/pulse; (c) 0.5mJ/pulse; (d) 1 mJ/pulse; (e) 2mJ/pulse; (f) 3mJ/pulse

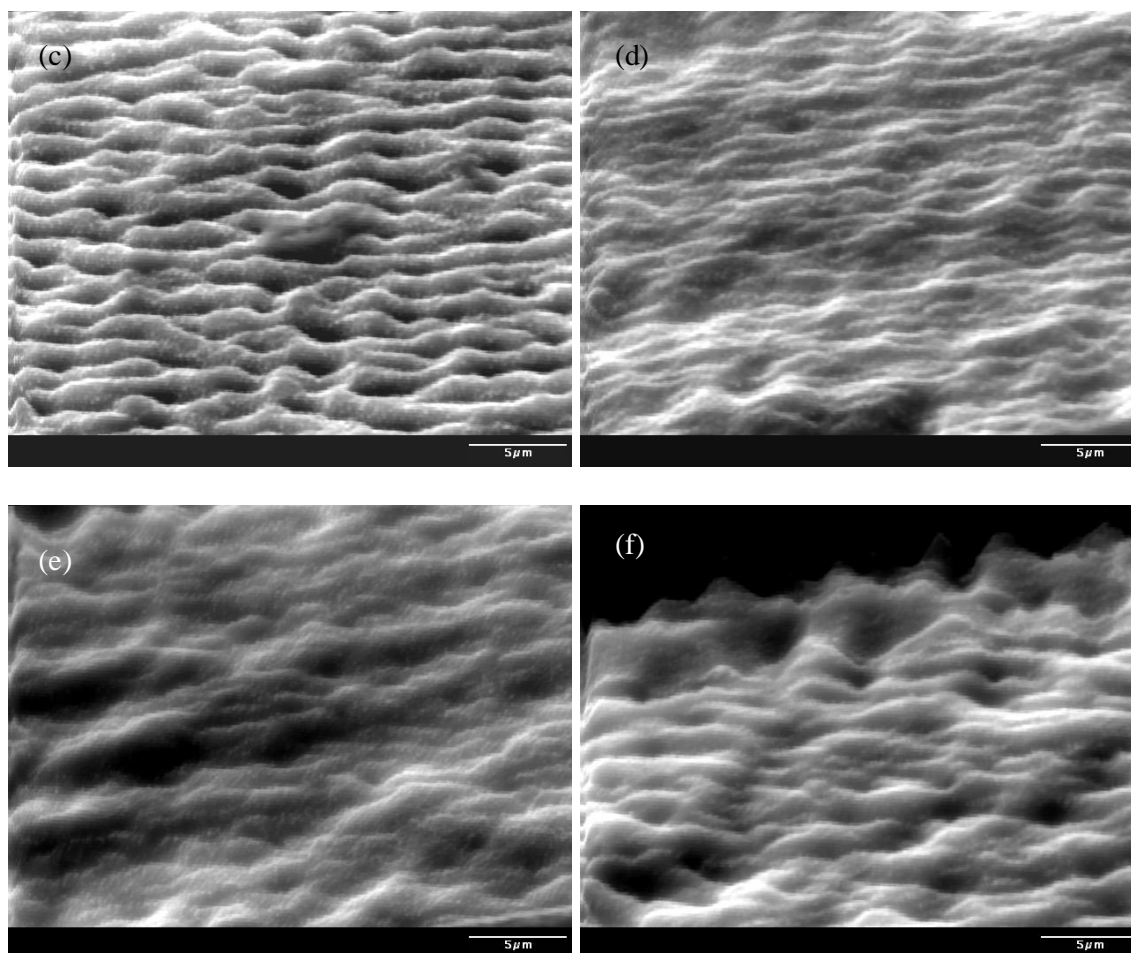


Figure 4.9. SEM images surface pattern formed in water by laser energy (a) 0.06mJ/pulse; (b) 0.16mJ/pulse; (c) 0.5mJ/pulse; (d) 1 mJ/pulse; (e) 2mJ/pulse; (f) 3mJ/pulse (cont.)

The evolution of structures in the air after irradiation by different laser powers has a similar trend as that in the water. Figure 4.10 shows the surface pattern images formed in the air. Obvious material damage does not occur at 0.06 mJ/pulse. As the pulse energy goes up to 0.16 mJ, variously sized bumps are caused by the interference among the incident laser and the surface waves. The interference effect becomes stronger, causing the heights and diameters of the bumps to grow. At 1 mJ/pulse laser energy, typical cone structures with tiny nano-particles on the cone surface protrude out of the material base.

The interference effect is the most pronounced in this case. Standing waves distributed on the surface are the cause of the periodic distributed cone structures. When the laser energy increases to 2mJ and 3mJ per pulse, the surface periodic structures disappear. Instead, some irregular pits and bumps and nano-particles dominate the surface because the laser power is so high that the wave interference effect can be totally ignored. Laser energy damage is the main cause of the surface roughness in this case. The nano-particle formation is subject to the material re-deposition effect. The higher the power is, the more obviously the effect acts.

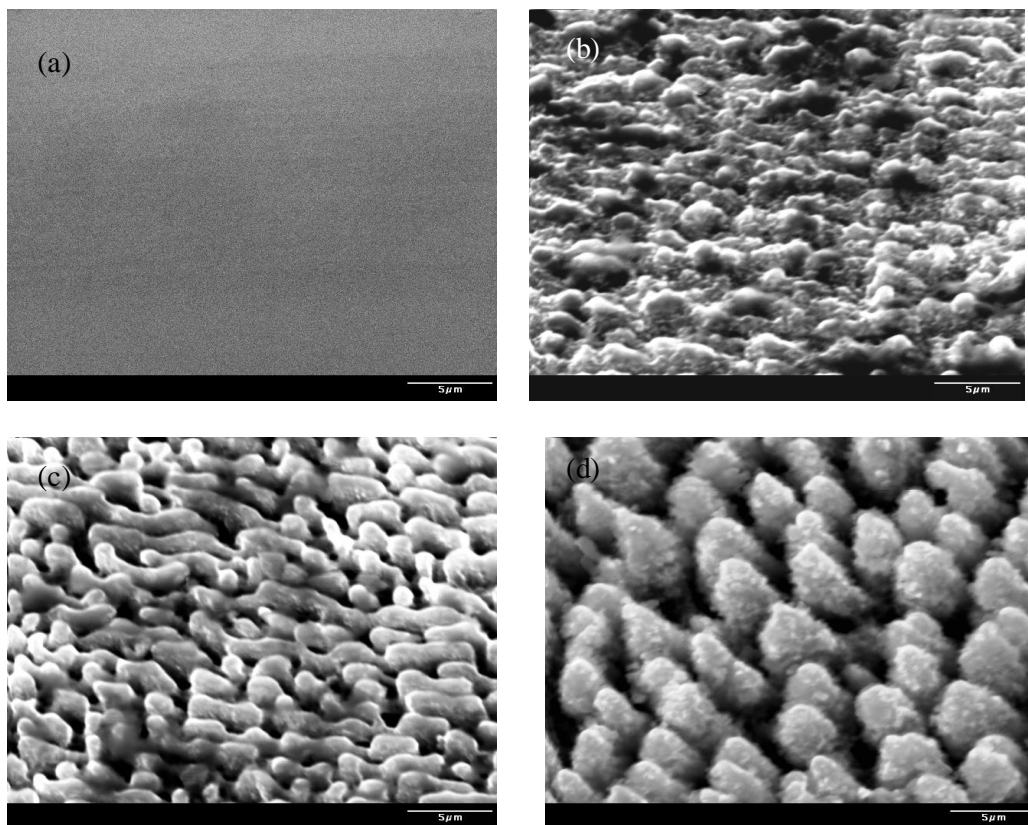


Figure 4.10. SEM images surface pattern formed in air by laser energy of (a) 0.06mJ/pulse; (b) 0.16mJ/pulse; (c) 0.5mJ/pulse; (d) 1 mJ/pulse; (e) 2mJ/pulse; (f) 3mJ/pulse

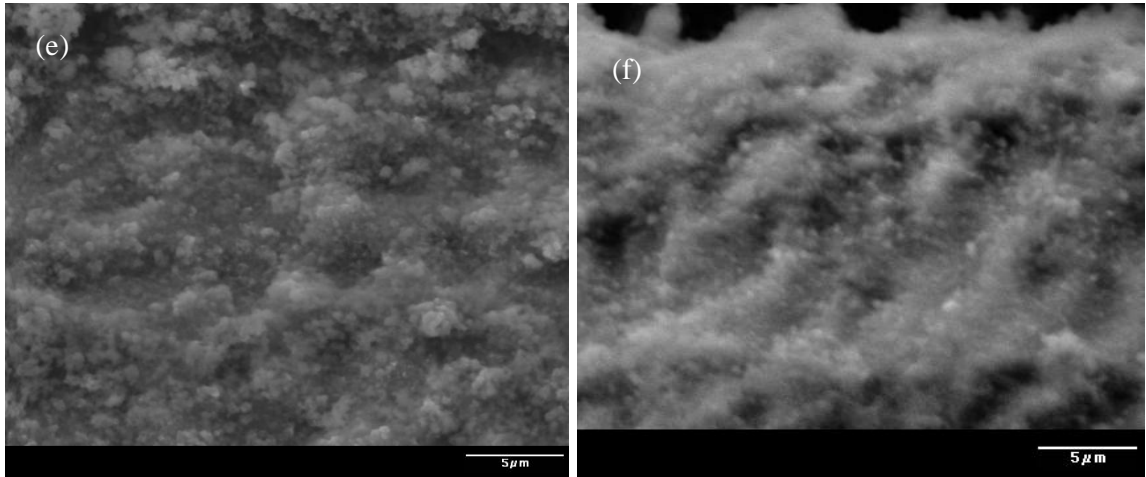


Figure 4.10. SEM images surface pattern formed in air by laser energy (a) 0.06mJ/pulse; (b) 0.16mJ/pulse; (c) 0.5mJ/pulse; (d) 1 mJ/pulse; (e) 2mJ/pulse; (f) 3mJ/pulse (cont.)

Basically, the evolution of surface patterns under different laser powers either in the water or in the air goes through a similar process: no damage on the surface, irregular patterns caused by weak wave interference, periodic patterns by strong wave interference, then large-power-induced bulk material breakdown.

4.3. EFFECT OF ANNEALING AND ETCHING

In practice, post-processing is usually applied following laser micromachining to alter the surface pattern. Annealing and chemical etching are two typical methods of post-processing. This section discusses the effects of annealing and etching on the surface pattern.

4.3.1. Annealing. The annealing approach has been applied to both the surface of periodic cones irradiated by laser in the air and the smooth surface irradiated by laser in the water. The manner in which annealing changes the microstructure morphology is analyzed and the potential of applying annealing to improve surface quality for industrial applications is studied.

The melting point of silicon is 1414 °C. The annealing temperature was set at 1100 °C and the annealing time at 3 hours for both in air and in water environments.

Figure 4.11 (a) and (b) are the SEM images of the surface pattern obtained in the air before and after annealing.

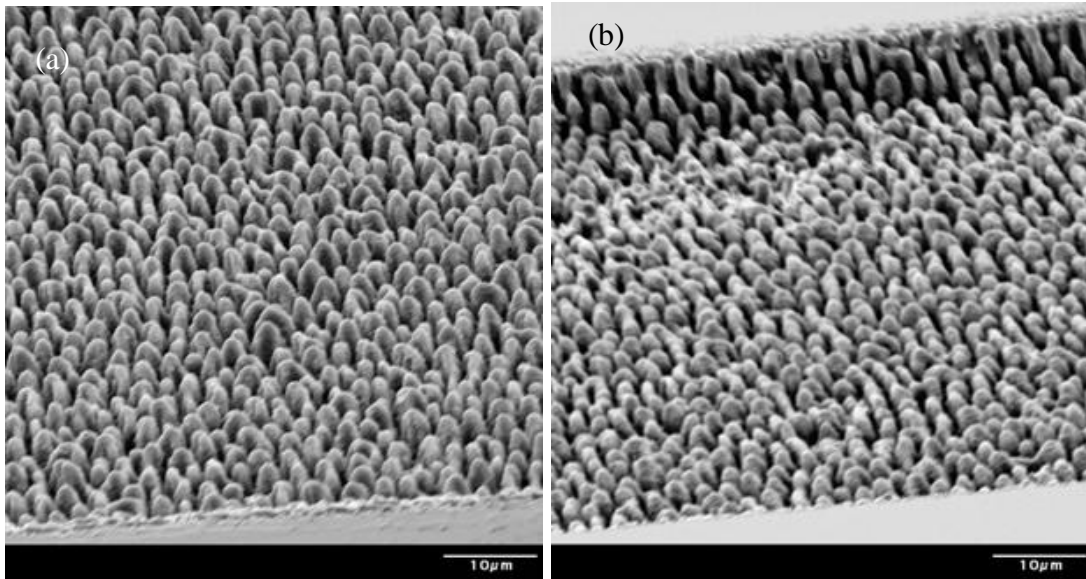


Figure 4.11 SEM images of microstructures on silicon surface in the air (a) before annealing at 1100 °C for 3 hours, (b) after annealing at 1100 °C for 3 hours.

No morphological difference is significantly visible within SEM image resolution. The columnar spikes after annealing seem to be shorter in height and have a blunter tip. Femtosecond laser-material interaction is a highly non-equilibrium process. Annealing leads to the diffusion of atoms within bulk material so that the material progresses towards its equilibrium state. The movement of atoms has the effect of redistributing and destroying the dislocations in order to relieve the internal stresses caused by non-equilibrium thermodynamic process. The height decrease and diameter increase of the cones after annealing is the result of the atoms redistributing to their equilibrium positions. Because of the existence of oxygen in the annealing oven, surface oxidation also causes the growth of the column diameters.

Figure 4.12 (a) and (b) are SEM images of the surface pattern obtained in the water before and after annealing. Tiny surface corrugations on the original surface grew to be quite rough. Material oxidation and surface atom re-distribution are the main causes of the roughness growth. Figure 4.13 is the EDS analysis result of the annealed sample. Except for Si, the percentage of oxygen was about 16%, which was much higher than that in the sample processed in the air. It verifies that the oxidation likely caused the roughness growth.

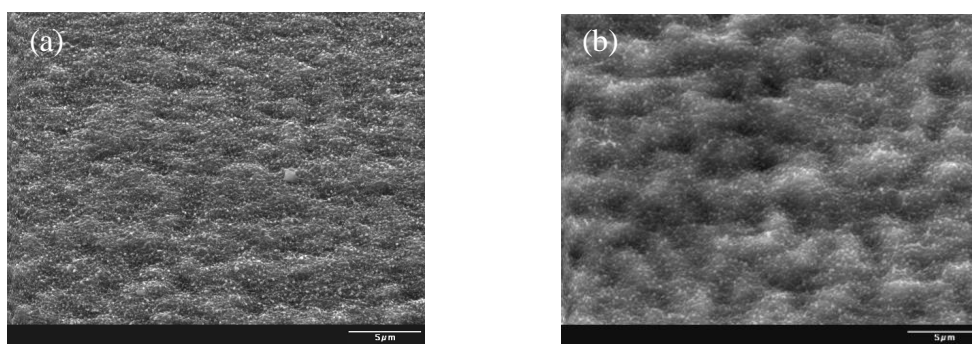


Figure 4.12 SEM images of surface morphology in the water (a) before annealing for 3 hours at 1100 °C, (b) after annealing for 3 hours at 1100 °C

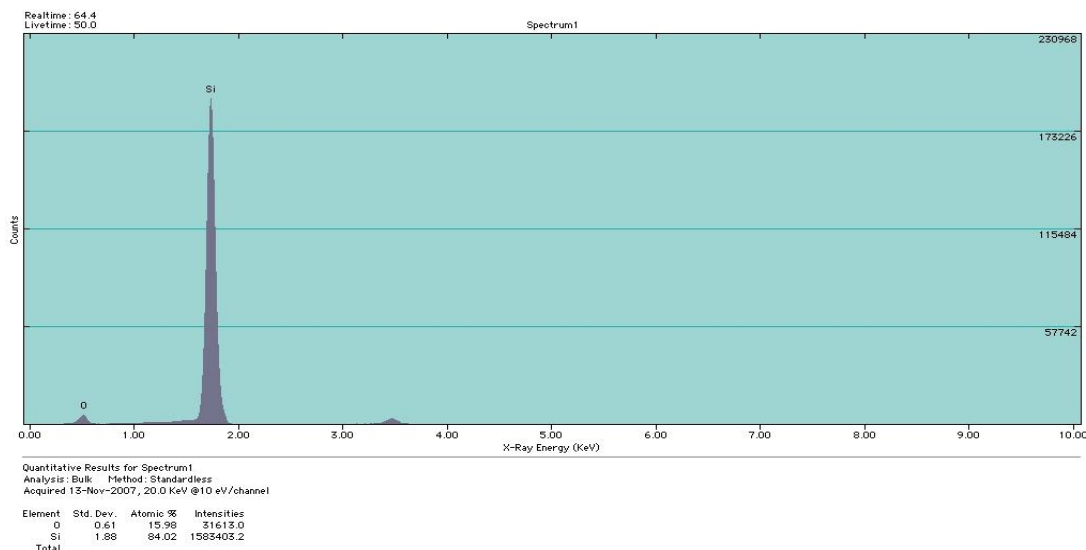


Figure 4.13 EDS analysis of the processed surface after annealing

4.3.2. Chemical Etching. HF etching is an effective approach to removing the surface oxide, thereby making the laser irradiated surface smoother [Shen et al., 2004]. HF and SiO₂ react, resulting in a SiF₄ solution, as shown in equilibrium equation (4.1).



According to previous EDS analysis, the oxide dominates the laser irradiated surface layer both in the air and in the water. Thus, the samples were etched in a 5% HF solution for 5 minutes to study the process of oxide removal.

Figure 4.14 compares the original surface after laser scanning in the air with the surface after HF etching. Overall, the shapes of the columnar spikes were not significantly different. Close investigation reveals that the surface of the spikes appears to be smoother after etching. This fact verifies that the nano-sized particles deposited on columnar spikes are oxide. Since the particles were resolved by the HF solution, the

interior silicon bulk, which is smooth, was revealed. The diameter of the spikes was also smaller after HF etching. The surface oxide removal caused the diameter of the spikes to shrink. Therefore, they look slimmer than those on the surface without HF etching.

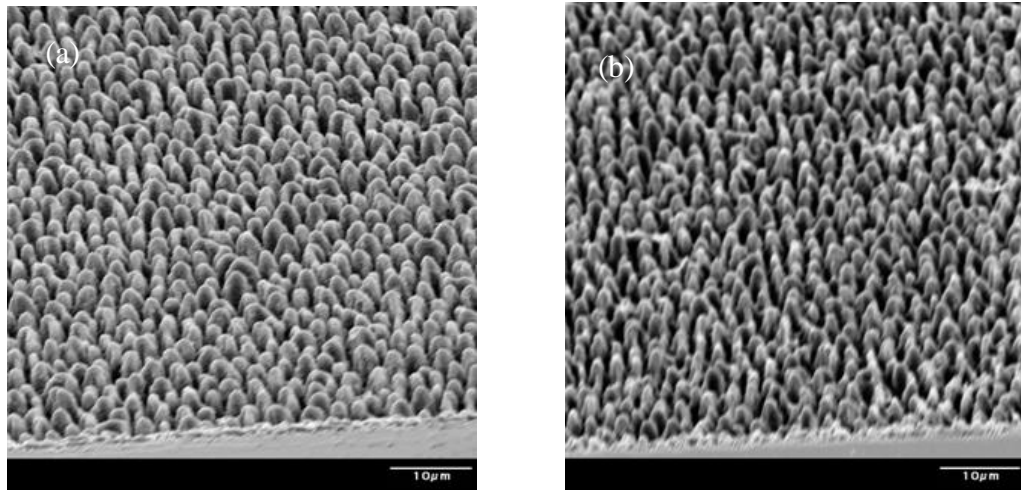


Figure 4.14 SEM images of microstructures on silicon surface in the air (a) before 5% HF etching for 5 minutes, (b) after 5% HF etching for 5 minutes.

Figure 4.15 (a) and (b) are SEM images of the surface pattern obtained in the water before and after HF etching. The surface was much cleaner after etching. The nanoparticles formed on the original surface were removed by HF erosion. From the EDS analysis shown in Figure 4.16, the content of oxygen after etching is less than that of the regular sample without etching.

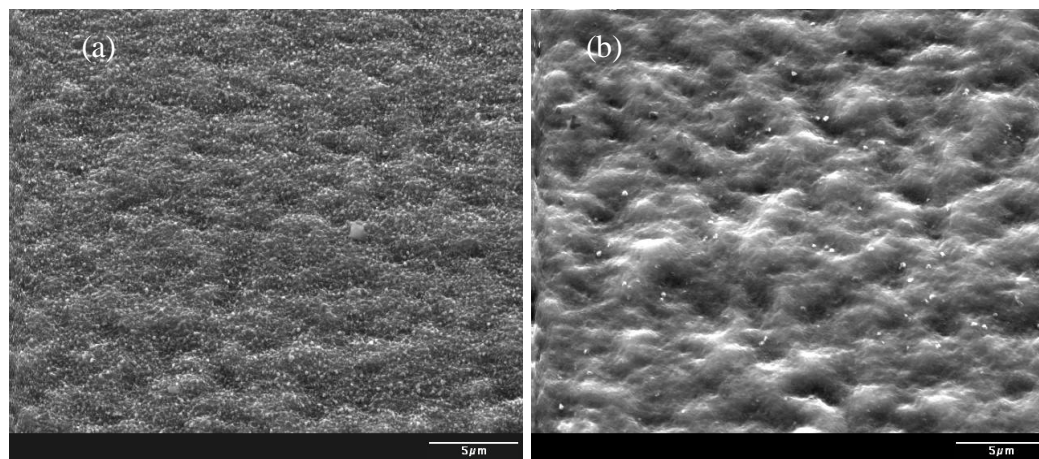


Figure 4.15 SEM images of microstructures on silicon surface in the water (a) before 5% HF etching for 5 minutes, (b) after 5% HF etching for 5 minutes

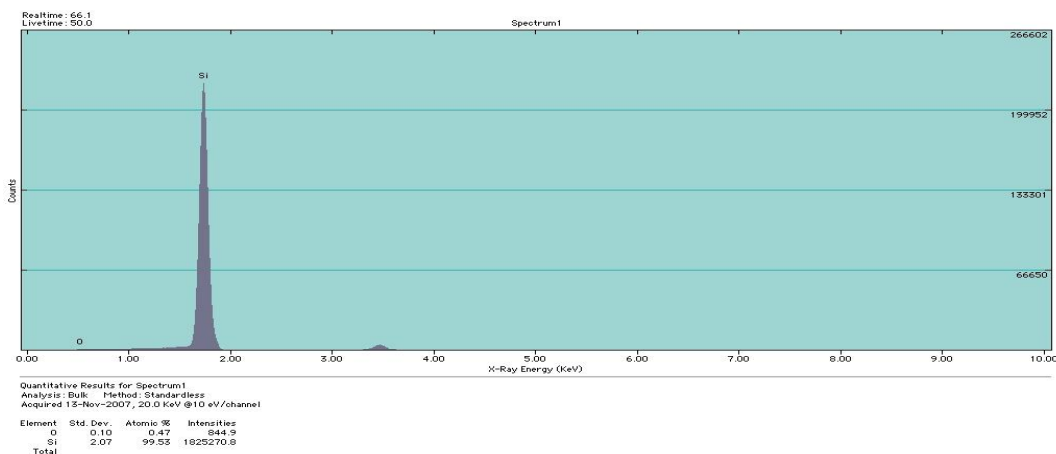


Figure 4.16 EDS analysis of the processed surface after etching

4.4. SUMMARY OF SURFACE MORPHOLOGY INDUCED BY LASER DIRECT WRITING

First, the laser repetition rate played a pronounced role in surface morphology induced by laser direct writing in water confinement. 100Hz was the threshold laser

repetition rate, at which a smooth surface was achieved, due to a special interference effect among laser light, bubble-induced mechanical waves and surface waves. Below 100 Hz, the laser overlapping was not sufficient to ablate the entire surface. Parallel ripples, with the distances of about 1.5 μm , dominated. Above this threshold, unevenly distributed pit-and-boulder structures formed. For the high repetition rate, laser-plasma absorption induced material damage overwhelmed the wave interference effect, contributing to rougher surfaces. In contrast, in the air laser repetition rate does not obviously affect the periodic columnar structures.

Second, by varying the laser power, the laser-induced periodic columns in the air environment evolved in the process of the column base formation, column body growth, column, and finally surface particle formation to column breakdown. The interference effect in the water was quite different from that in the air due to bubble formation. At a certain median laser power, the ripple-like periodic structures formed. Below this power, the surface looked smooth; above it, the ripples gradually broke down into irregular pits and bumps with considerable roughness.

Third, the post processing of samples acted to modify the surface to some extent. Annealing served to redistribute the atoms to their equilibrium positions. For the samples processed in the air, the periodic columns appeared to be blunter and shorter after annealing. For the samples processed in the water, the surface oxidation phenomenon was pronounced, which made the surface become rough. HF etching resolved the surface oxide effectively. Hence, the diameters of the columns decreased, and the column surface

appeared to be smoother after etching for the surface scanned by the laser in the air. For the case in the water, the surface was clean after etching, and all the the nano-particles deposited on the original surface were removed.

5. CONCLUSION AND OUTLOOK

This dissertation examines femtosecond laser micromachining of silicon in water confinement. Analysis of the surface morphology and the underlying physical mechanism has been presented. The results should serve as a valuable reference in the application of femtosecond lasers in the micro-machining industry.

First, laser ablation experiments were carried out to study the basic physics underlying laser-material interaction process. In the laser power experiment, the laser ablation threshold was first tested for a single pulse shot in water of 0.03mJ, which was the same as that in air. As laser power went up, the two-region crater-shaped structures dominated both in the water and in the air. At a very high power level, the morphology evolved into flower-like corrugations ablated in the water, while still remained as two-region craters in the air. The theoretical single pulse ablation threshold and laser focal radius were calculated by extrapolating the fitting curve of crater diameter versus laser power.

In focal position experiment, a sequence of co-central periodic ring structures appeared both in the water and in the air due to shock waves as the laser beam focused beneath the water-material surface. Because the focus was quite near the surface, flower-like rough corrugations and two-region craters were dominant in both the water and in the air. As the focal position moved above the surface, flower-like corrugations and two-regional craters gradually diminished.

In the laser shot number experiment, the incubation theory was proposed to explain the energy accumulation process of multi-pulse of ablation, which leads to the increase in the diameter and depth of the laser-induced craters.

Another important aspect of this dissertation is its study of the surface pattern after laser direct scanning. Since the goal was to apply a femtosecond laser to fabricate a device by direct writing, a good surface quality is compulsory.

By changing the laser repetition rate but fixing the traveling speed, the effect of repetition rate on the morphology was studied. The threshold repetition rate was found to be 100 Hz, at which a smooth silicon surface can be achieved in the water. The interference among laser light, bubble-induced mechanical waves, and surface waves was proposed as the cause of this phenomenon. Below 100 Hz, parallel ripple-like waves, with the distance about 1.5 μm , dominated. Above this threshold, unevenly distributed rough pit-and-boulder structures formed. In contrast, in the air, repetition rate does not obviously affect the periodic columnar structures on the surface.

When the laser power was increased, the laser-induced surface pattern in the water experienced tiny damage on the surface, worm-like ripples, rough pits, and bumps after ripple breakdown. However, in the air environment, the surface pattern evolved in the process of the column base formation, body growth, surface particle formation, and finally, breakdown at last.

A post processing experiment was also applied. Annealing makes the periodic columns blunter and shorter in the air due to atom redistribution. It causes severe oxidation and, thereby, surface roughness in the water confinement. HF solution etching caused the columnar surface to be smoother and the diameter of the columns to decrease

in the air. For the case in the water, the surface became clean due to oxidation removal after etching.

The periodic structures seen on the silicon surface in the air are seldom detected in the water because the bubble formation alters the interference of laser light and surface waves. At a certain laser repetition rate, the surface roughness can be dramatically lowered to a level that meets industrial requirement. The surface quality can be further improved by proper post-processing.

Although we achieved a bunch of interesting and useful experimental results were achieved, further insightful study of the formation mechanism of laser-water-material interaction process is still needed. I suggest a further numerical modeling study, such as MD or ab-initio modeling, be carried out in order to simulate the fundamental physics phenomenon during the laser-material interference process. Such modeling must be conducted in order to effectively control and understand the laser micromachining process under water.

BIBLIOGRAPHY

Aggarwal, S., Monga, A., P., Perusse, S., R., Ramesh, R., Ballarotto, V., Williams, E., D., Chalamala, B., R., Wei, Y., Reuss, R., H.,: Spontaneous ordering of oxide nanostructures, *Science*, 287, 2235-2237, 2000

Baudach, S., Bonse, K., Kautek, W.,: Ablation experiments on polyimide with Femtosecond laser pulses, *Appl Phys A* 69, S395-S398, 1999

Ben-Yakar, A., Byer, R., L., Harkin, A., Ashmore, J., Stone, H., A.,: Morphology of femtosecond laser ablated borosilicate glass surfaces, *Appl Phys Letters* , 83, 3030-3032, 2003

Bensner, S., Degorce, J., Kabashin, A., Meunier, M.,: Influence of ambient on femtosecond laser processing of silicon, *Applied Surface Science*, 247, 163-168, 2005

Bonse, J., Munz, M., Sturm, H.,: Structure formation on the surface of indium phosphide irradiated by femtosecond laser pulses, *Journal of Applied Physics*, 97, 013538-013538-9 2005

Bonse, J., Baudach, S., Krüger, J., Kautek, W., Lenzner, M.,: Femtosecond laser ablation of silicon-modification thresholds and morphology, *Applied Physics, A* 74, 19-25, 2002

Bonse, J., Sturm, H., D. Schmidt., Kautek, W.,: Chemical, morphological and accumulation phenomena in ultrashort-pulse laser ablation of TiN in air, *Applied Physics, A* 71, 657-665, 2000

Bonse, J., Geuß, M., Baudach, S., Sturm, H., Kautek, W.,: The precision of the femtosecond-pulse laser ablation of TiN films on silicon, *Appl. Phys., A* 69, S399-S402, 1999

Bonse, J., Wrobel, J., Krüger, J., Kautek, W., Ultrashort-pulse laser ablation of indium phosphide in air, *Appl. Phys., A* 72, 89-94 , 2001

Borowiec, A., Haugen, H., K.,: Subwavelength ripple formation on the surface of compound semiconductors irradiated with femtosecond laser pulses, *Appl. Phys. letters*, 82, 4462-4464, 2003

Borowiec, A., Mackenzie, M., Weatherly, G., C., Haugen, H., K.,: Transmission and scanning electron microscopy studies of single femtosecond-laser-pulse ablation of silicon, *Appl Phys A* 76, 201-207, 2003

Borowiec, A., Mackenzie, M., Weatherly, G., C., Haugen, H., K.: Femtosecond laser pulse ablation of GaAs and InP: studies utilizing scanning and transmission electron microscopy, *Appl Phys A* 77, 411-417, 2003

Cahill, D., G., Yalisove, S., M.: Ultrafast lasers in materials research, *MRS Bulletin*, 31, 594-600, 2006

Carey, J.: Femtosecond-laser Microstructuring of Silicon for Novel Optoelectronic Devices, Ph.D Thesis, Harvard University, 2004

Carey, J., E., Crouch, C., H., Shen, M., Mazur, E.: Visible and near-infrared responsivity of femtosecond-laser microstructured silicon photodiodes, *Optics Letters*, 30, 1773-1775, 2005

Cerami, L., Mazur, E., Nolte, S., Schaffer, C.: Femtosecond laser micromachining, Draft 6.4 of 6/14/2007

Chen, K., Ihlemann, J., Simon, P., Baumann, I., Sohler, W., Generation of submicron surface gratings on LiNbO₃ by ultrashort UV laser pulses, *Appl. Phys. A* 65, 517-518, 1997

Costache, F., Henyk, M., Reif, J., Surface patterning on insulators upon femtosecond laser ablation, *Applied Surface Science*, 208-209, 486-491, 2003

Costache, F., Kouteva-Arguirova, S., Reif, J.: Sub-damage-threshold laser ablation from crystalline Si: surface nanostructures and phase transformation, *Appl. Phys. A* 79, 1429-1432 (2004)

Coyne, E., Magee, J., P., Mannion, P., O'Connor, G., M., Glynn, T., J., Characterization of laser ablation of silicon using a Gaussian wave front and computer generated wave front reconstruction, *Appl Surface Science*, 229, 148-160, 2004

Coyne, E., Magee, J., P., Mannion, P., O'Connor, G., M., Glynn, T., J., STEM (scanning transmission electron microscopy) analysis of femtosecond laser pulse induced damage to bulk silicon, *Appl. Phys. A* 81, 371-378, 2005

Crouch, C., Carey, J., Warrender, J. Aziz, M. Mazur, E., Infrared absorption by sulfur-doped silicon formed by femtosecond laser irradiation, *Applied Physics*, A79, 1635-1641, 2004

Crouch, C., Carey, J., Shen, M. Mazur, E., Génin, F., Comparison of Structure and properties of femtosecond and nanosecond laser-structured silicon, *Applied Physics Letters*, 84, 1850-1852, 2004

- Crouch, C., H., Carey, J., E., Shen, M., Mazur, E., Genin, F., Y.,: Infrared absorption by sulfur-doped silicon formed by femtosecond laser irradiation, *Appl Phys A*, 79, 1635-1641, 2004
- Daminelli, G., Krüger, J., and Kautek, W., Femtosecond laser interaction with silicon under water confinement, *Thin Solid Films*, 467, 334-341, 2004
- Dong, Y., Molian, P.,: Femtosecond pulsed laser ablation of 3C-SiC thin film on silicon, *Appl Phys A* 77, 839-846, 2003
- Dong, Y., Zorman, C., Molian, P.,: Femtosecond laser micromachining of single crystalline 3C-SiC structures based on a laser-induced defect-activation process, *Journal of Micromech. Microeng.* 13, 680-685, 2003
- Dumitru, G., Romano, V., Gerbig, Y., Weber, H., P., Haefke, H.,: Femtosecond laser processing of nitride-based thin films to improve their tribological performance, *Appl Phys A* 80, 283-287, 2005
- Dumitru, G., Romano, V., Weber, H., P., Sentis, M., Marine, W.,: Femtosecond ablation of ultrahard materials, *Appl Phys A* 74, 729-739, 2002
- Emel'yanov, V., Babak, D., Defect capture under rapid solidification of the melt induced by the action of femtosecond laser pulses and formation of periodic surface structures on a semiconductor surface, *Appl. Phys. A* 74, 797-805, 2002
- Ezaki, Mizunori., Kumagai, Hiroshi., Tyoda, Koichi., Obara, Minoru., Dot Structures Fabricated by Laser Etching -Laser Wavelength Dependence of Dot Structures Fabricated by Laser Etching, *Jpn. J. Appl. Phys.*, 32, 1308-1311, 1993
- Furusawa, K., Takahashi, K., Kumagai, H., Midorikawa, K., Obara, M.,: Ablation characteristics of Au, Ag, and Cu metals using a Femtosecond Ti:sapphire Laser, *Appl. Phys. A* 69, S359-S366, 1999
- Georgescu, I., Pattern formation upon femtosecond laser ablation of transparent dielectrics, Diploma Thesis, Brandenburgische Technische Universität Cottbus, 2003
- Harzic, R., L., Schuck, H., Sauer, D., Anhut, T., Riemann, I., König, K.,: Sub-100nm nanostructuring of silicon by ultrashort laser pulses, *Optic Express*, Vol 13, No 17, 6651-6656, (2005)
- Henyk, M., Vogel, N., Wolframm, D.,: Femtosecond laser ablation from dielectric materials: Comparison to arc discharge erosion, *Appl Physics A* 69, S355-S358, 1999
- Her, T., H., Finlay, R., J., Wu, C., Mazur, E.,: Femtosecond laser-induced formation of spikes on silicon, *Appl Phys A* 70, 383-385 (2000)

- Her, T., Finlay, R., J., Wu, C., Deliwala, S.,: Microstructuring of silicon with femtosecond laser pulses, *Appl Phys Letters*, 73, 1673-1675, 1998
- Hwang, D., Choi, T., Grigoropoulos, C.,: Liquid-assisted femtosecond laser drilling of straight and three-dimensional microchannels in glass, *Appl. Phys. A79*, 605-612, 2004
- Jee, Y., Becker, M., Walser, R., Laser-induced damage on single-crystal metal surfaces., *J. Opt. Soc. Am.B*, 5, 648-659, 1988
- Jeoung, C., Kim, H., S., Park, M., Lee, J., Kim, C., S., Park, C.,: Preparation of room-temperature photoluminescent nanoparticles by ultrafast processing of single-crystalline Ge, *Japanese Journal of Appl Phys*, 44, 5278-5281, 2005
- Kasaai, R., Kacham, V., Theberge, F., Chin, S., The interaction of femtosecond and nanosecond laser pulses with the surface of glass, *Journal of Non-Crystalline Solids*, 319, 129-135, 2003
- Kautek, W., Phase Separations and Phase Changes by Ultrashort Pulse Lasers, *Thin Solid Films* 467, 334-336, 2004
- Kautek, W., Rudolph, P., Daminelli, G., Kruger, J.,: Physico-chemical aspects of femtosecond-pulse-laser-induced surface nanostructures, *Appl. Phys. A* 81, 65-70, 2005
- Kawamura, D., Takita, A., Hayasaki, Y., Nishida, N.,: Bump formation on a glass surface with a transparent coating using femtosecond laser processing, *Appl. Phys. A* 85, 39-43, 2006
- Kawamura, K., Sarukura, N., Hirano, M., Ito, N., Hosono, H.,: Periodic nanostructure array in crossed holographic gratings on silica glass by two interfered infrared-femtosecond laser pulses, *Appl. Phys. Letters* Vol 79, No9, 2001
- Kawamura, K., Motomitsu, E., Hirano, M., Hosono, H.,: Formation of microstructure in SiO₂ thin film by femtosecond laser pulse, *Japanese Journal of Appl. Phys. A* Vol 41, 4400-4403, 2002
- Kim, D., Ye, M., Grigoropoulos, C.,: Pulsed laser-induced ablation of absorbing liquids and acoustic-transient generation, *Applied Physics A* 67, 169-181, 1998
- Klein-Wiele, J., H., Bekesi, J., Simon, P.,: sub-micron patterning of solid materials with ultraviolet femtosecond pulses, *Appl. Phys. A* 79, 775-778, 2004
- Koch, J., Korte, F., Fallnich, C., Ostendorf, A., Chichkov, B., N.,: Direct-write subwavelength structuring with femtosecond laser pulses, *Optical Engineering* 44(5), 051103-051103-5, 2005

Kondo, T., Matsuo, S., Juodkazis, S., Mizeikis, V., Misawa, H.,: Multi photon fabrication of periodic structures by multibeam interference of femtosecond pulses, *Appl Phys letters* , 82, 2758-2760, 2003

Korte, F., Koch, J., Chichkov, B., N.,: Formation of microbumps and nanojets on gold targets by femtosecond laser pulses, *Appl Phys A* 79, 879-881, 2004

Korte, F., Serbin, J., Koch, J., *et al.*, Towards nanostructuring with femtosecond laser pulses, *Appl. Phys. A*77, 229-235, 2003

Matsuo, S., Juodkazis, S., Misawa, H.,: Femtosecond laser microfabrication of periodic structures using a microlens array, *Appl Phys A* 80, 683-685, 2005

Magyar, J., Aita, C., Gajdardziska-Josifovska, M., Sklyarov, A., Mikhaylichenko, K., Yakovlev, V., V.,: High-power laser interactions with nanostructured materials, *Appl. Phys. A* 77, 285-291, 2005

Mannion, P., Magee, J., Coyne, E., O'Connor, G., Glynn, T., The effect of damage accumulation behaviour on ablation thresholds and damage morphology in ultrafast laser micro-machining of common metals in air, *Applied surface Science*, 233, 275-287, 2004

Matsumura, T., Kazama, A., Yagi, T.,: Generation of debris in the femtosecond laser machining of a silicon substrate, *Appl. Phys. A* 81, 1393-1398, 2005

Mills, J., D., Kazansky, P., G., Bricchi, B., Baumberg, J.,: Embedded anisotropic microreflectors by femtosecond-laser nanomachining, *Appl Phys Letters*, 81, 196-198, 2002

Miyazaki, K., Maekawa, N., Kobayashi, W., Kaku, M., Yasumaru, N., Kiuchi, J.,: Reflectivity in femtosecond-laser-induced structural changes of diamond-like carbon film, *Appl. Phys., A* 80, 17-21, 2005

Nakata, Y., Okada, T., Maeda, M.,: Lithographical laser ablation using femtosecond laser, *Appl Phys, A* 79, 1481-1483, 2004

Nayak, B., Gupta, M., Kolasinski, K.,: Spontaneous formation of nanospiked microstructures in germanium by femtosecond laser irradiation, *Nanotechnology*, 18, 195302-195302-4, 2007

Okamoto, T., Ohmura, E., Sano, T., Morishige, Y., Miyamoto, I.,: Analytical study on metal microstructures using femtosecond laser, *Appl. Phys. A* 81, 639-643, 2005

Ozkan, A., M., Malshe, A., P., Railkar, T., A., Brown, W., D., Shrik, M., D., Molian, P., A.,: Femtosecond laser-induced periodic structure writing on diamond crystals and microclusters, *Appl Phys letters* , Vol 75, 1703-1705, 1999

Perez, D., Lewis, L., Molecular-dynamics study of ablation of solids under femtosecond laser pulses, *Physical Review B* 67, 184102-184102-15, 2003

Pedraza, A., J., Fowlkes, J., D., Lowndes, D., H.,: Self-organized silicon microcolumn arrays generated by pulsed laser irradiation, *Appl. Phys. A*, 69, S731-S734, 1999

Pedraza, A., J., Fowlkes, J., D., Lowndes, D., H.,: Silicon microcolumn arrays grown by nanosecond pulsed-excimer laser irradiation, *Appl. Phys. Letters*, 74, 2322-2324, 1999

Pereira, A., Cros, A., Delaporte, P., Georgiou, S., Manaousaki, A., Marine, W., Sentis, M.,: Surface nanostructuring of metals by laser irradiation: effects of pulse duration wavelength and gas atmosphere, *Appl. Phys. A* 79, 1433-1437, 2004

Podlipensky, A., Abdolvand, A., Seifert, G., Graener, H.,: Femtosecond laser assisted production of dichroitic 3D structures in composite glass containing Ag nanoparticles, *Appl. Phys., A* 80, 1647-1652, 2005

Qian, H., Zhou, W., Zheng, H., Lim, G., Morphological and chemical evolution on InP(100) surface irradiated with femtosecond laser, *Surface Science*, 595, 49-55, 2005

Qian, H., Zhou, W., Zheng, H., Ripple Formation on InP surface Irradiated with femtosecond laser, *International Journal of Nanoscience*, 4, 779-784, 2005

Ramanathan, D., Molian, P., A.,: Micro-and sub-miromachining of type IIa single crystal diamond using a Ti:Sapphire femtosecond laser, *Journal of Manufacturing Science and engineering* , 124, 389-396, 2002

Riedel, D., Hernandez-Pozos, J., L., Palmer, R., E., Kolasinski, K., W.,: Fabrication of ordered arrays of silicon cones by optical diffraction in ultrafast laser etching with SF₆, *Appl. Phys., A* 78, 381-385, 2004

Salle, B., Gobert, O., Meynadier, P., Perdrix, M., Petite, G., Semerok, A.,: Femtosecond and picosecond laser microablation: Ablation efficiency and laser microplasma expansion, *Appl. Phys., A* 69, s381-s383, 1999

Sanchez, F., Morenza, J., L., Aguiar, R., Delgado, J., C., Varela, M.,: Whiskerlike structure growth on silicon exposed to ArF excimer laser irradiation, *Appl. Phys. Letters*, 69 (5), 620-622, 1996

Schaffer, C., Interaction of femtosecond laser pulses with transparent materials, Ph.D. Thesis. Harvard University, 2001.

Segawa, H., Yoshida, K., Kondo, T., Kondo, T., Matuso, S., Misawa, H.,: Fabrication of Photonic Crystal Structures by Femtosecond Laser- Induced Photopolymerisation of Organic-Inorganic Film, *Journal of Sol-Gel Science and Technology*, 26, 1023-1027, 2003

Segawa, H., Matsuo, S., Misawa, S.: Fabrication of fine-pitch TiO₂-organic hybrid dot arrays using multi-photon absorption of femtosecond pulses, *Appl. Phys., A* 79, 407-409, 2004

Seifert, G., Kaempfe, M., Syrowatka, F., Harnagea, C., Hesse, D., Graener, H.: Self-organized structure formation on the bottom of femtosecond laser ablation craters in glass, *Appl. Phys., A* 81, 799-803, 2005

Seo, M., A., Kim, D., S.: Polarization-induced size control and ablation dynamics of Ge nanostructures formed by a femtosecond laser, *Optic Express* Vol 14, No.8, 3694, 2006

Sheehy, M., A., Winston, L., Carey, J., E., Friend, C., M., Mazur, E.: Role of background gas in the morphology and optical properties of laser-microstructured silicon, *Chem. Mater.*, 17, 3582-3586, 2005

Shen, M., Y., Crouch, C., H., Carey, J., E., Mazur, E.: Femtosecond laser-induced formation of submicrometer spikes on silicon in water, *Appl. Phys. Letters*, 85, 5694-5696, 2004

Shen, M., Y., Crouch, C., H., Carey, J., E., Younkin, R., Mazur, E., Sheehy, M., Friend, C., M.: Formation of regular arrays of silicon microspikes by femtosecond laser irradiation through a mask, *Appl. Phys. Letters*, 82, 1715-1717, 2003

Shimotsuma, Y., Hirao, K., Kazansky, P., G., Qiu, J.: Three dimensional micro and nano-fabrication in transparent materials by femtosecond laser, *Japanese Journal of Appl. Phys. Letter.*, 44, 4735-4748, 2005

Sipe, J., Young, J., Preston, J., Driel, H.: Laser-induced periodic surface structure. I. Theory, 27, 1141-1154, 1983

Simakin, A., V., Voronov, V., V., Kirichenko, N., A., Shafeev, G., A.: Nanoparticles produced by laser ablation of solids in liquid environment, *Appl. Phys., A* 79, 1127-1132, 2004

Spie, J., E., Young, J., F., Preston, J., S., Van Driel, H., M.: Laser-induced periodic surface structure. I. Theory, *Physical Review B* 27, 1141-1154, 1983

Sylvestre, J., P., Kabashin, A., V., Sacher, E., Meunier, M.: Femtosecond laser ablation of gold in water: influence of the laser-produced plasma on the nanoparticle size distribution, *Appl. Phys. A* 80, 753-758, 2005

Tan, B., Venkatakrishnan, K., A femtosecond laser-induced periodical surface structure on crystalline silicon, *Journal of Micromechanics and Microengineering.*, 16, 1080-1085, 2006

Thøerge, F., Chin, S., L.: Enhanced ablation of silica by the superposition of femtosecond and nanosecond laser pulses, *Appl. Phys. A* 80, 1505-1510, 2005

- Theppakuttai, S., Chen, S., Submicron ripple formation on glass surface upon laser-nanosphere interaction, *Journal of Applied Physics*, 95, 5049-5052, 2004
- Tran, D., Zheng, H., Lam, Y., Murukeshan, V., Chai, J., Hardt, D., Femtosecond laser-induced damage morphologies of crystalline silicon by sub-threshold pulses, *Optics and Lasers in Engineering*, 43, 977-986, 2005
- Tran, D., Lam, Y., Zheng, H., Murukeshan, V., Chai, J., Hardt, D., Femtosecond laser processing of crystalline silicon, *Proceedings of The 5th Singapore-MIT Alliance Annual Symposium*, Singapore, 19-20 January 2005
- Tull, B., R., Carey, J., E., Sheehy, M., A., Friend, C., Mazur, E.,: Formation of silicon nanoparticles and web-like aggregates by femtosecond laser ablation in a background gas, *Appl. Phys. A* 83, 341-346, 2006
- Tull, B., R., Carey, J., E., Mazur, E., McDonald, J., P., Yalisove, S., M.,: Silicon surface morphologies after femtosecond laser irradiation, *MRS Bulletin Vol 31*, 2006
- Vasquez, M., j., Halada, G., P., Clayton, C., R., Gouma, P., I.,: Fabrication of nanostructured Al₂CuMg thin film by femtosecond pulsed laser ablation, *Thin Solid Films*, 458, 37-42, 2004
- Venkatakrishnan, K., Sivakumar, N., Hee C., Tan, B., Liang, W., Gan, G., Direct fabrication of surface-relief grating by interferometric technique using femtosecond laser, *Appl. Phys.*, A77, 959-963, 2003
- Wagner, R., S., Ellis, W., C.,: Vapor-liquid-solid mechanism of single crystal growth, *Appl. Phys. Letters*, 4, 89-90, 1964
- Wang, J., Guo, C.,: Formation of extraordinary uniform periodic structures on metals induced by Femtosecond laser pulses, *Journal of Applied Physics*, 100, 023511-023511-4, 2006
- Wang, C., Z., Ho, K., M., Shirk, M., D., Molian, P., A.,: Laser-induced graphitization on a diamond(111) surface, *Phys. Review Letters*, 85, 4092-4095, 2000
- Wang, C., Lim, G., Ng, F., Liu, W., Chua, S., Sub-wavelength periodic ripple formation on GaN sapphire by femtosecond laser pulses, SIMTech technical reports, 6, 35-39, 2005
- Watanabe, Kumiya., Cahill, David., Gundrum, Bryan., and Averback, R.S., Ablation of Crystalline Oxides by Infrared Femtosecond Laser Pulses, *Journal of Applied Physics*. 100, 083519-083519-6, 2006
- Wu, C., Crouch, C., Zhao, L. Mazur, E., Visible Luminisence from silicon surfaces microstructured in air, *Applied Physics Letters*, 81, 1999-2001, 2002

Wu, Z., Jiang, H., Zhang, Z., Sun, Q., Yang, H., Morphological investigation at the front and rear surfaces of fused silica processed with femtosecond laser pulses in air, *Optics Express*, 10, 1244-1249, 2002

Yang, G.,: Laser ablation in liquids: Applications in the synthesis of nanocrystals, *Progress in Materials Science*, 52, 648-698, 2007

Yasumaru, N., Miyazaki, K., Kiuchi, J.,: Fluence dependence of Femtosecond-Laser-induced nanostructure formed on TiN and CrN, *Appl. Phys. A* 81, 933-937, 2005

Yasumaru, N., Miyazaki, K., Kiuchi, J.,: Glass carbon layer formed in diamond-like carbon films with femtosecond laser pulses, *Appl. Phys. A* 79, 425-427, 2004

Yasumaru, N., Miyazaki, K., Kiuchi, J.,: Femtosecond-laser-induced nanostructure formed on hard thin films of TiN and DLC, *Appl. Phys. A* 76, 983-985, 2003

Younge, J., F., Preston, J., S., Van Driel, H., M., Spie, J., E.,: Laser induced surface periodic structure. II Experiments on Ge, Si, Al and brass, *Physical Review B* 27, 1155-1172, 1983

Younkin, R., Carey, J., E., Mazur, E., Levinson, J., A., Friend, C., M.,: Infrared absorption by conical silicon microstructures made in a variety of background gases using femtosecond-laser pulses, *Journal of Appl. Phys. A* 93, 2626-2629, 2003

Zhang, G., Gu, D., Jiang, X., Chen, Q., Gan, F., Femtosecond laser pulse irradiation of Sb-rich AgInSbTe films: Scanning electron microscopy and atomic force microscopy investigations, *Appl. Phys. A* 80, 1039-1043, 2005

Zheng, H., Y., Zhou, W., Qian, H., X., Tan, T., T., Lim, G., C.,: Polarisation-independence of femtosecond laser machining of fused silica, *Appl. Surface Science*, 236, 114-119, 2004

Zhou, Guosheng., Fauchet, P., Siegman A., Growth of spontaneous periodic surface structures on solids during laser illumination. *Physical Review B* 26, 5366-5381, 1982

VITA

Songping Wu was born in Wuhan, China on May 9, 1981. He attended Wuhan University from 1999 to 2003 and received the degree of Bachelor of Science in Materials Science & Engineering and Computer Science in 2003. He attended Huazhong University of Science & Technology from 2003 to 2006 and received a Master of Science in Material Science & Engineering. He began to work toward another Master of Science in Mechanical Engineering at the University of Missouri-Rolla (now Missouri University of Science & Technology), USA, in the Fall of 2006 and received a Master's in May 2008.